Title	Studies on Novel Catalysts for Direct Decomposition of Nitrogen Monoxide Based on Rare Earth Oxides
Author(s)	辻本, 総一郎
Citation	大阪大学, 2014, 博士論文
Version Type	VoR
URL	https://doi.org/10.18910/34431
rights	
Note	

Doctoral Dissertation

Studies on Novel Catalysts for Direct Decomposition of Nitrogen Monoxide Based on Rare Earth Oxides

(希土類酸化物を母体とした新規な一酸化窒素直接分解触媒に関する研究)

Soichiro Tsujimoto

January 2014

Department of Applied Chemistry
Graduate School of Engineering
Osaka University

Studies on Novel Catalysts for Direct Decomposition of Nitrogen Monoxide Based on Rare Earth Oxides

(希土類酸化物を母体とした新規な一酸化窒素直接分解触媒に関する研究)

2014

Soichiro Tsujimoto

Department of Applied Chemistry
Graduate School of Engineering
Osaka University

Preface

The work of this thesis has been carried out under the supervision of Professor Dr. Nobuhito Imanaka at Department of Applied Chemistry, Graduate School of Engineering, Osaka University.

The object of this thesis is to elucidate the factors of catalytic direct NO decomposition and propose a mechanism for NO decomposition over a catalyst based on C-type cubic rare earth oxides.

The author wishes that the findings of this study provide useful suggestions and information for further development and establishment of novel catalysts.

Soichiro Tsujimoto

Soichiro Tsujimoto

Department of Applied Chemistry
Graduate School of Engineering
Osaka University
2-1Yamadaoka, Suita, Osaka 565-0871
Japan

January 2014

Contents

Chapter 1

Fundamental Factors for Rare Earth Oxides to Exhibit Direct NO Decomposition Catalysis

Chapter 2

Effects of the Introduction of Alkaline Earth Metal and Terbium Ions on the NO Decomposition Activity of C-type Cubic Y_2O_3

Chapter 3

Mechanism for Direct NO Decomposition over the Catalysts Based on C-type Cubic Y_2O_3

Chapter 4

Evaluation of Catalytic Activity for Direct NO Decomposition over C-type Cubic REOs-Based Catalysts and Synthesis of Advanced Catalysts to Inhibit Catalyst Poisoning by O_2 and CO_2

General Introduction

Nitrogen oxides (NO_x) are not only harmful to the human body but are also responsible for photochemical smog and acid rain when present in relatively large quantities [1, 2]. Emission sources of NO_x can be divided into mobile and fixed sources. Automobiles and marine vessels are well known examples of mobile sources, while the large-scale boilers used in factories are fixed sources. To remediate NO_x from automobile exhausts, the three-way catalyst (TWC) and NO_x storage reduction (NSR) catalyst are applied, while to remove NO_x emitted from fixed sources, selective catalytic reduction (SCR) processes using ammonia is typically used [3, 4].

The TWC is an effective system for gasoline-engine vehicles, in which the oxygen concentration in the exhaust gas can be controlled, but is unsuitable for diesel engines because oxygen exists relatively at high concentrations. For the NSR catalysts, NO_x gases are eliminated in a reductive atmosphere by supplying a large quantity of fuel to the engines to produce fuel-rich conditions, thereby reducing the gas mileage [5]. For fixed sources, SCR methods employing ammonia are effective, having sufficient decomposition efficiency and a stable reaction process at high temperatures [6–13]. However, separate specialized equipment is needed to supply the ammonia and it is absolutely essential to ensure secure control systems because of the high toxicity and flammability of ammonia. Although SCR systems using an aqueous solution of urea have been practically applied in diesel-engine vehicles [14–18], an additional anti-icing system such as a heater is necessary in cold climates because the urea solution freezes at below −11°C.

In contrast to the above methods, direct decomposition of NO_x offers an ideal and reasonable route for NO removal because there is no need to add toxic reducing agents such as ammonia, urea and hydrocarbon. In this process, the NO_x gases are decomposed into nitrogen (N_2) and oxygen (O_2) as harmless atmospheric components by simple contact with the catalyst surfaces. Accordingly, direct NO_x decomposition catalysts offer considerable advantages with respect to both environmental and economic considerations.

In the early 1990s, it was found that Cu ion-exchange zeolites (Cu-ZSM-5) showed high NO decomposition activity at temperatures in the range of 400 − 500 °C [19]. Up to date, no catalysts have shown activities as high as those of Cu-ZSM-5 in the moderate temperature range. However, they lack hydrothermal stability at elevated temperatures and are deactivated irreversibly above 600 °C. In contrast, perovskite-type oxides were found to become active above 500 °C and exhibit catalytic activities in the high-temperature region from 500 − 800 °C [20−22]. However, the reaction is strongly inhibited by the presence of oxygen and carbon dioxide.

To address these issues, the Imanaka laboratory, to which I belong, has focused on C-type cubic rare earth sesquioxides, R_2O_3 (R: rare earths), as novel catalysts for direct NO decomposition [23, 24]. At temperatures lower than approximately 2000 °C, three crystal polymorphs are known to exist for rare earth sesquioxides, namely A-type hexagonal, B-type monoclinic, and C-type cubic (**Figure G-1**), according to the ionic size of the respective rare earth elements [25].

The A-type of hexagonal sesquioxides is of space group *P32/m* with one formula per unit cell [26]. The metal ions are in a seven coordination with four oxide anions closer than the other three. The four oxide anions are bonded to five metals and the other three to four metal ions.

The B-type sesquioxides is formed as a monoclinic distortion of the A-type. The B-type structure has the space group *C2/m* with six formulas units per cell [27]. The metal ions in the B-type polymorph are located in six- and seven-coordination sites.

The C-type structure is of the cubic bixbyite type structure, cubic space group, *Ia3*, containing 32 metal atoms and 48 oxygen atoms per unit cell [28] related to a double-edge fluorite structure with one-fourth of the oxygen sites vacant and regularly ordered (**Figure G-2)**. The metal ions are located in six-coordination sites in this structure. The lattice volume of the C-type structure is larger than those of A-type and B-type ones (**Figure G-3**). In other words, C-type structure possesses large interstitial open spaces in its structure, which have been identified to play an important role in the direct NO decomposition in our laboratory [23, 24].

Figure G-4 shows the temperature ranges of stability of the three polymorphic forms. For La_2O_3 and Nd_2O_3, the A-type structure is stable up to about 2000 °C under ordinary pressure, although the C-type samples have been reported in some special cases [29, 30]. For Sm_2O_3, the B-type and the A-type structures are thermodynamically stable, and the B to A transition is occurred above 1835 °C [31]. Ce, Pr, and Tb ions can take both trivalent and tetravalent oxidation states and thereby they form intermediate compounds in narrow composition ranges with the generic formula Ln_nO_{2n-2m} (n is an integer or infinity and m is between 1 and 8). Accordingly, it is difficult to obtain the C-type oxide in a single phase form in air. In contrast, Eu_2O_3, Gd_2O_3, Dy_2O_3, Ho_2O_3, Y_2O_3, Er_2O_3, Tm_2O_3, Yb_2O_3, and Lu_2O_3 can adopt the C-type structure stably up to at least 1000 °C.

During my research work, I found that a $(Y_{0.69}Tb_{0.30}Ba_{0.01})_2O_{2.99+\delta}$ catalyst, in which some of the Y^{3+} sites in Y_2O_3 were substituted with $Tb^{3+/4+}$ and Ba^{2+}, exhibited high NO decomposition activity. Using this oxide, 100 % NO decomposition into N_2 and O_2 was realized for the first time at 900 °C, a level of decomposition which was not achieved by the conventional perovskite-type catalysts. The introduction of oxide anion vacancies by partial substitution of the Y^{3+} sites with divalent Ba^{2+} ions should improve the catalytic activity of Y_2O_3, because oxide anion vacancies are active sites for NO adsorption and decomposition [21]. The redox properties of $Tb^{3+/4+}$ may also be the reason for the improvement of the catalytic activity, because reduction of the tetravalent cation to the trivalent state promotes O_2 desorption from the catalyst surface [32] to regenerate the active sites for direct NO decomposition.

However, the reaction mechanism of the direct NO decomposition over the C-type cubic rare earth oxides still remains to be clarified. The specific reasons why the C-type structure is favorable to exhibit high catalytic activity have not been understood, and the fundamental roles of the dopants to enhance the catalytic activity have not been clarified in detail yet.

Therefore, the present study aims to elucidate the factors of direct NO decomposition over the rare earth oxides (REOs). To this end, the effects of dopants and several physicochemical properties on the NO decomposition activity of the C-type cubic REOs were investigated. Based on these considerations, a catalytic reaction mechanism for direct NO decomposition over the C-type cubic REO catalysts was proposed. Furthermore, the catalytic performance test was carried out in the presence of various inhibition gases to evaluate durability of the C-type REO catalysts against CO_2 and O_2.

This thesis consists of the following four chapters.

Chapter 1 deals with the fundamental factors for REOs to exhibit direct NO decomposition catalysis. A causal relationship between crystal structure and catalytic activity was defined based on the NO adsorption ability of the respective REOs. Subsequently, the effects of several possible factors for NO decomposition such as the number of basic sites, lattice parameter, and morphology, were investigated.

In **Chapter 2**, the effects of the introduction of alkaline earth ions (Ba^{2+}, Sr^{2+}, and Ca^{2+}) and $Tb^{3+/4+}$ on the NO decomposition activity of C-type cubic Y_2O_3 were discussed from the aspect of the basicity and O_2 desorption behavior of the catalysts.

In **Chapter 3**, a reaction mechanism was proposed for the direct NO decomposition catalysis over the C-type cubic REOs. The adsorbed species at high temperatures were identified to understand the surface reaction during the NO decomposition.

In **Chapter 4**, the NO decomposition behavior of the $(Y_{0.69}Tb_{0.30}Ba_{0.01})_2O_{2.99+\delta}$ catalyst was characterized in detail and the catalytic activities in the presence of CO_2 or O_2 were compared with those of the conventional catalysts. Furthermore, some advanced catalysts were produced for the direct NO decomposition even in the presence of CO_2 or O_2, not only by the introduction of the rare earth ions that show redox property, but also by the purpose exclusion of alkaline earth ions from the catalyst lattice.

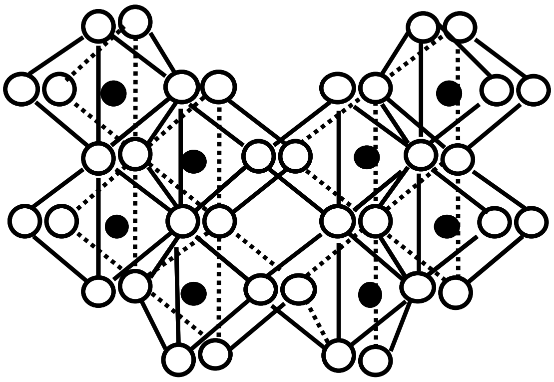

A-type hexagonal (*P32/m*)

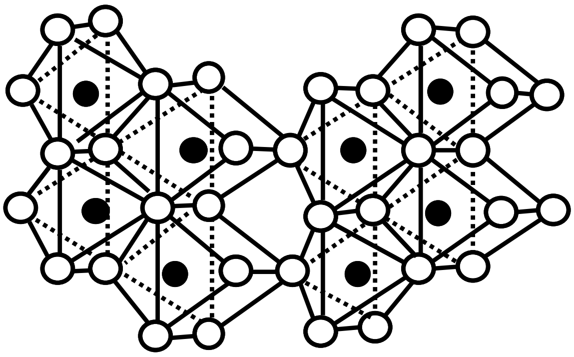

B-type monoclinic (*C2/m*)

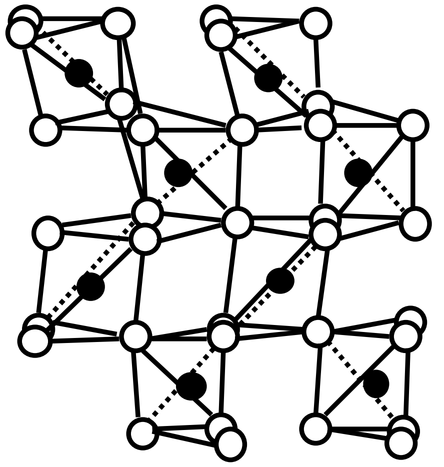

C-type cubic (*Ia3*)

Figure G-1 Representative of A-type, B-type, and C-type R_2O_3. The solid dots and open dots indicate the metal atoms and oxide atoms, respectively.

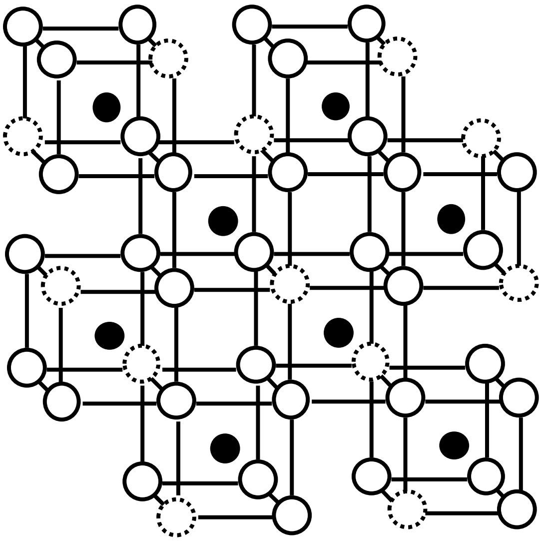

Cubic fluorite structure

-1/4 O^{2-}

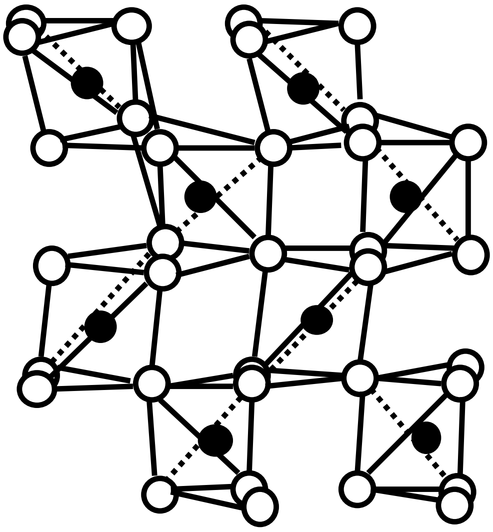

C-type cubic structure

Figure G-2 The relationship between the cubic fluorite oxide (RO_2; R: rare earths) and the C-type cubic bixbyite sesquioxide (R_2O_3). The solid dots and open dots indicate the metal atoms and oxide atoms, respectively. Removal of one-quarter of the oxygen atoms of the fluorite-type oxide along nonintersecting strings in the four (1 1 1) directions results in the formation of the C-type structure.

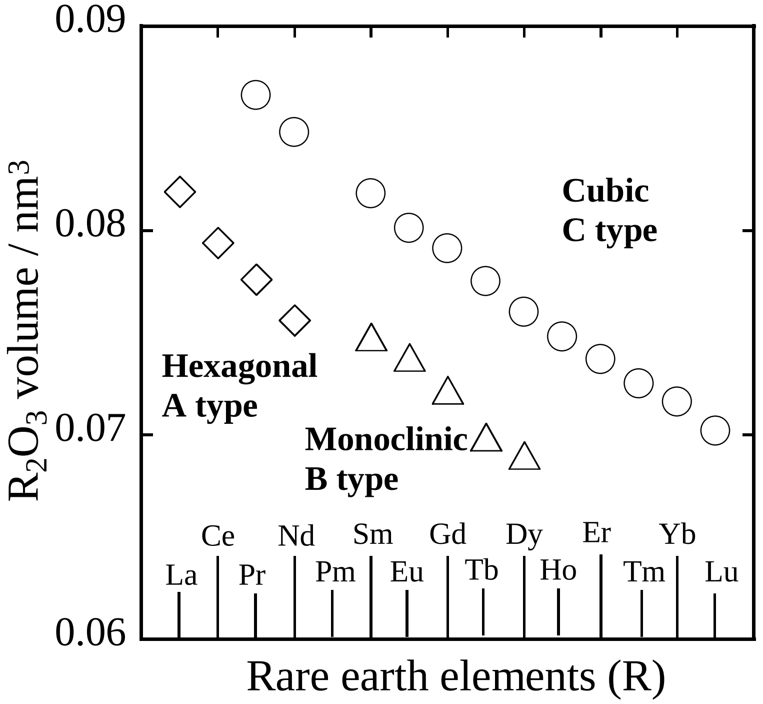

Figure G-3 Lattice volume of rare earth sesquioxides.

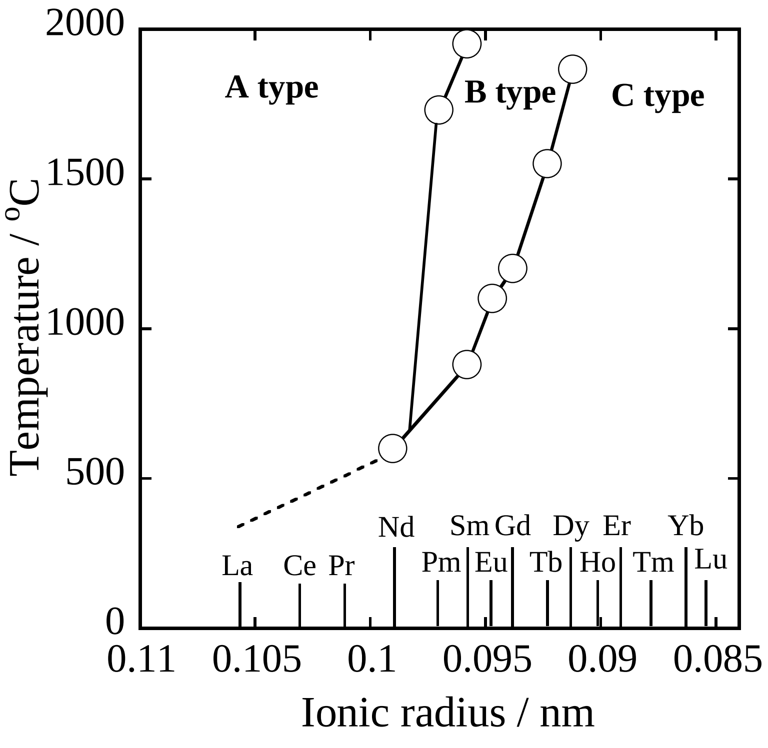

Figure G-4 Polymorphic transformation for the rare earth sesquioxides.

List of Publications

1. Direct Decomposition of NO on C-type Cubic Rare Earth Oxides Based on Y_2O_3,

   Soichiro Tsujimoto, Koji Mima, Toshiyuki Masui, Nobuhito Imanaka

   Chemistry Letters, 2010, **39(5)**, 456–457.

2. Direct Decomposition of NO into N_2 and O_2 on C-type Cubic Y_2O_3-ZrO_2 and Y_2O_3-ZrO_2-BaO,

   Soichiro Tsujimoto, Xiaojing Wang, Toshiyuki Masui, Nobuhito Imanaka

   Bulletin of the Chemical Society of Japan, 2011, **84(7)**, 807–811.

3. Coexisting Gas-resistant C-type Cubic Yb_2O_3-Tb_4O_7 Catalysts for Direct NO Decomposition,

   Soichiro Tsujimoto, Chiya Nishimura, Toshiyuki Masui, Nobuhito Imanaka

   Chemistry Letters, 2011, **40(7)**, 708–710.

4. Effects of Tb and Ba Introduction on the Reaction Mechanism of Direct NO Decomposition over C-type Cubic Rare Earth Oxides Based on Y_2O_3,

   Soichiro Tsujimoto, Keisuke Yasuda, Toshiyuki Masui, Nobuhito Imanaka

   Catalysis Science & Technology, 2013, **3(8)**, 1928–1936.

5. Direct Decomposition of Nitrogen Monoxide on (Ho, Zr, Pr)$_2$O$_{3+\delta}$ Catalysts,

   Soichiro Tsujimoto, Chiya Nishimura, Toshiyuki Masui, Nobuhito Imanaka

   Catalysis Communications, 2014, **43**, 84–87.

6. Direct Decomposition of Nitrogen Monoxide over C-type Cubic Y_2O_3-Pr_6O_{11} Solid Solutions

   Soichiro Tsujimoto, Toshiyuki Masui, Nobuhito Imanaka

   RSC Advances, 2014, **4**, 1146–1149.

7. Fundamental Factors for Rare Earth Oxides to Exhibit Direct NO Decomposition Catalysis.

   Soichiro Tsujimoto, Toshiyuki Masui, Nobuhito Imanaka

   in contribution.

Supplementary Publication

1. Direct Decomposition of NO into N_2 and O_2 over C-Type Cubic Y_2O_3-Tb_4O_7-ZrO_2,

   Toshiyuki Masui, Shunji Uejima, Soichiro Tsujimoto, Nobuhito Imanaka

   Materials Sciences and Applications, 2012, **3(10)**, 733–738.

Chapter 1 Fundamental Factors for Rare Earth Oxides to Exhibit Direct NO Decomposition Catalysis

1.1 Introduction

As mentioned in the General Introduction, REOs are the most attractive candidates for novel direct NO decomposition catalysts [23, 24]. However, there are no systematic studies on the fundamental factors for pure REOs to exhibit direct NO decomposition activity, and the crucial roles of the crystal structure on the NO decomposition remains unclear. In addition, catalytic activity of heterogeneous catalysts generally relates to the physicochemical characteristics of the catalyst surface [33−35]. In most cases, in particular, the catalytic activity is significantly affected by the morphology of the catalyst particle at the microscopic level [36−38]. Furthermore, during my research work, I have recently demonstrated that control of the surface basicity of the catalyst is also important to enhance the NO decomposition activity.

In this chapter, therefore, A-type, B-type, C-type, and fluorite-type REOs were synthesized and the structure dependence on the NO decomposition activity was discussed from the standpoint of the coordination environment of the rare earth ions in each crystal structure. In order to better understand the factors that contribute to the NO decomposition catalysis, surface basicity, lattice parameter, and morphology of the C-type cubic REOs were characterized and their relationships to the NO decomposition activities were investigated.

1.2 Experimental Procedure

All REOs samples were synthesized by a carbonate precipitation method. Aqueous solutions of 1.0 mol dm^{-3} $R(NO_3)_3$ (R: rare earths) was added to a 1.0 mol dm^{-3} ammonium carbonate solution with stirring. The pH of the mixture was adjusted to 10 by dropwise addition of an ammonia solution. After stirring for 6 h, the resulting precipitate was collected by filtration, washed several times with deionized water, and then dried at 80 °C for 6 h. The powder was then ground in an agate mortar and finally calcined at 900 °C in air for 6 h. In the case of Sm_2O_3, the precursor was calcined at 1000 °C in air for 6 h to obtain the sample in a single phase form of the B-type monoclinic structure.

The samples were characterized using X-ray powder diffraction (XRD; Rigaku, SmartLab) with Cu-Kα radiation. XRD patterns were recorded in the 2θ range from 10° to 70°. The specific surface area was measured using the Brunauer-Emmett-Teller (BET) method by nitrogen adsorption at −196 °C with an adsorption analyzer (Micromeritics, Trister 3000). Fourier transform-infrared spectroscopy (FT-IR) measurements were performed with an FT-IR spectrophotometer (Bruker Optics, Tensor 27) in a dry atmosphere at room temperature. The samples were ground and mixed with KBr at a 1/10 ratio (w/w), and the mixture was then pressed into a thin disc. A clean KBr disc was used as a reference. Electron spin resonance (ESR) spectra were recorded with an ESR spectrometer (Bruker Optics, ELEXSYS E500). The magnetic field was scanned from 3200 to 3700 Gauss. The microstructure of the catalysts was observed with a scanning electron microscope (SEM; Shimadzu, SSX-550) operating with an accelerating voltage of 12 kV. The sample was sputter-coated with a platinum layer before SEM observation to avoid any possible surface charging effects. Transmission electron microscopic images were also taken with an accelerating voltage of 300 kV (TEM; Hitachi H-9000NAR).

The number of basic sites of the REOs was estimated from the temperature-programmed desorption (TPD) profiles of CO_2, assuming that one CO_2 molecule adsorbs on one basic site. The sample was heated in a flow of H_2 (30 cm^3 min^{-1}) at 600 °C for 30 min to avoid O_2 evolution caused by the reduction of rare earth ions during the measurement process. The REOs was next cooled in a flow of He to 50 °C and then exposed to CO_2 (1 atm) at this temperature for 1 h, so that all the basic sites were covered with CO_2 molecules. After evacuation at 50 °C for 30 min, the catalyst was heated under a flow of He at a rate of 10 °C min^{-1} and the desorbed gas was monitored using a gas chromatograph with a catalysis analyzer (BEL Japan, BELCAT-B).

The catalytic tests were carried out in a conventional fixed-bed flow reactor with a 10 mm-diameter quartz glass tube. A schematic view of the apparatus is shown in **Figure 1.1**. A gas mixture of 1.0 vol% NO and He (balance) flowed over 0.5 g of catalyst at a rate of 10 cm^3 min^{-1}. The *W/F* ratio, where *W* and *F* are the sample weight and gas flow rate, respectively, was adjusted to 3.0 g s cm^{-3}. The gas composition was analyzed using a gas chromatograph (Shimadzu, GC-8A) with a thermal conductivity detector (TCD) and a molecular sieve 5A column for NO, N_2, and O_2 separation. The activity of each catalyst was evaluated in terms of NO conversion to N_2.

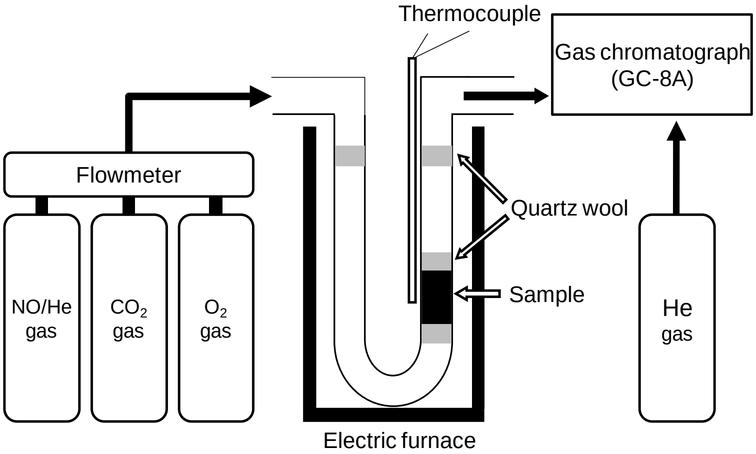

Figure 1.1 A schematic view of the catalyst performance testing apparatus for direct NO decomposition.

1.3 Results and Discussion

Figure 1.2 shows the XRD patterns of the REOs synthesized in this study. The crystal structures of La_2O_3 and Nd_2O_3 (**Figure 1.2 (a)**) were A-type hexagonal. The crystal structures of Sm_2O_3 and CeO_2 (**Figure 1.2 (b)**) were B-type monoclinic and cubic fluorite, respectively. Crystallites of Eu_2O_3, Gd_2O_3, Dy_2O_3, Ho_2O_3, Y_2O_3, Er_2O_3, Tm_2O_3, Yb_2O_3, and Lu_2O_3 had the C-type cubic structure (**Figure 1.2 (c)**). Crystal structures, BET surface areas, and lattice parameters estimated from the XRD patterns of these REOs are summarized in **Table 1.1**. The lattice parameters are in good agreement with those in a reference [25], but there is no clear relationship between the BET surface area and the lattice parameter.

NO_x species in the exhaust gas emitted at high temperatures are composed primarily of thermodynamically stable nitrogen monoxide (NO). Accordingly, studies concerning the catalytic NO_x removal usually focus on enhancing the conversion of NO. **Figure 1.3** shows the dependence of the rare earth elements on the NO conversion to N_2 at 900 °C on the REOs. The activity of each REO was measured after the samples were heated at 900°C for at least 2 hours. In the catalytic performance tests, N_2 formation derived from direct NO decomposition was detected for all samples, and higher N_2 yield was obtained for C-type cubic REOs than those for A-type hexagonal, B-type monoclinic, and cubic fluorite-type oxides. The reason for difference in the catalytic performance is not mainly due to the surface area, because there is no definite correlation between catalytic activity and surface area of the REOs as summarized in **Table 1.1**. Therefore, the high N_2 yield observed for the C-type cubic oxides could be attributed to the characteristics of its crystal structure.

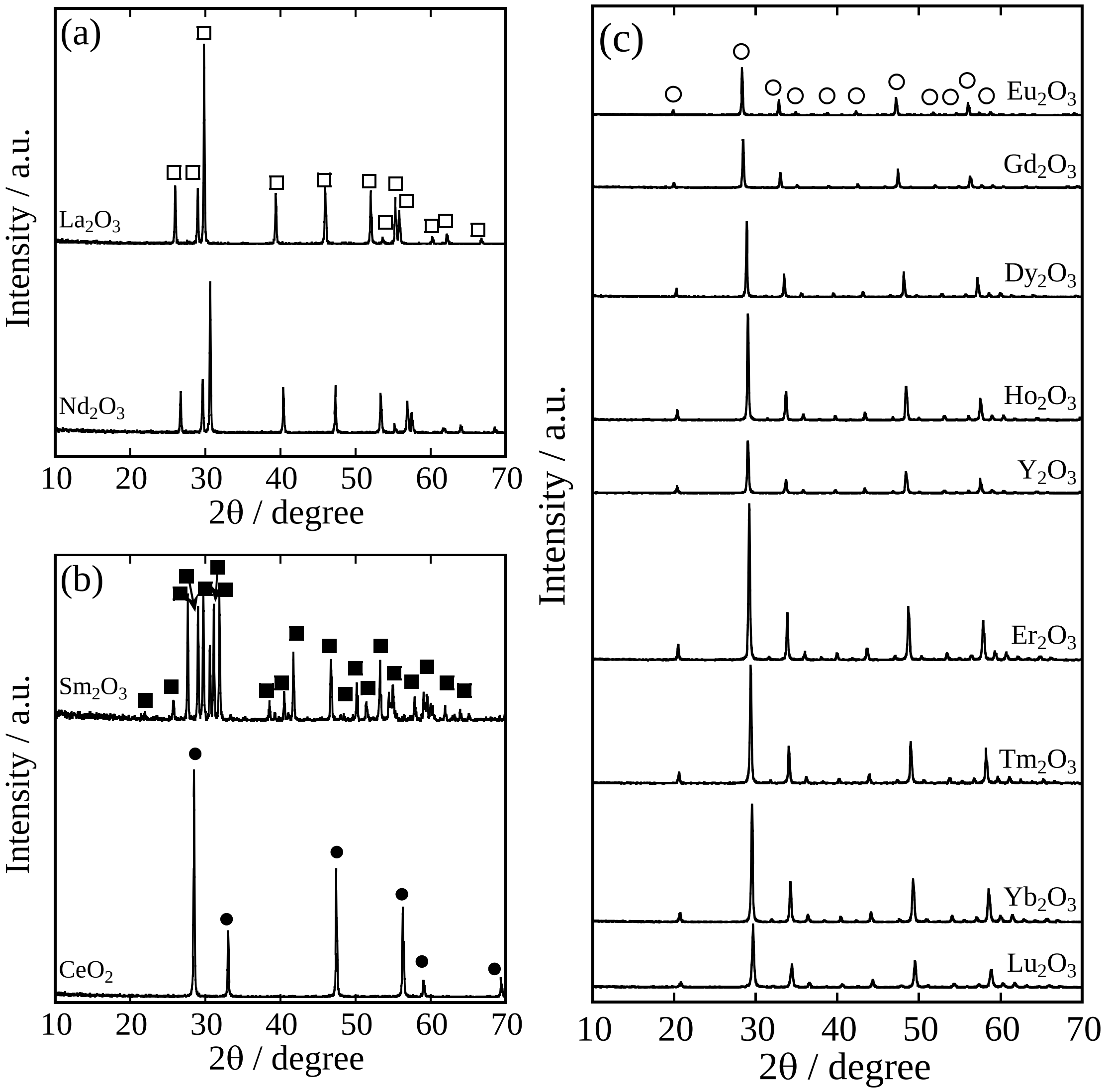

Figure 1.2 XRD patterns of (a) La_2O_3 and Nd_2O_3, (b) Sm_2O_3 and CeO_2, and (c) Eu_2O_3, Gd_2O_3, Dy_2O_3, Ho_2O_3, Y_2O_3, Er_2O_3, Tm_2O_3, Yb_2O_3, and Lu_2O_3. The open squares and solid squares indicate the A-type hexagonal and the B-type monoclinic phases, respectively. The open and solid dots indicate C-type cubic and cubic fluorite-type phases, respectively.

Table 1.1 Crystal structure, BET specific surface area, and lattice parameter of REOs

Rare earth oxide	Crystal structure	BET surface area / m^2 g^{-1}	Lattice parameter / nm
La_2O_3	A-type hexagonal	2.1	a = b = 0.3938 c = 0.6125
CeO_2	Cubic fluorite	4.1	1.0768
Nd_2O_3	A-type hexagonal	3.4	a = b = 0.3831 c = 0.5995
Sm_2O_3	B-type monoclinic	5.7	a = 1.4183 b = 0.3626 c = 0.8850
Eu_2O_3	C-type cubic	3.7	1.0867
Gd_2O_3	C-type cubic	4.8	1.0816
Dy_2O_3	C-type cubic	4.6	1.0664
Ho_2O_3	C-type cubic	5.1	1.0607
Y_2O_3	C-type cubic	13.3	1.0597
Er_2O_3	C-type cubic	8.2	1.0545
Tm_2O_3	C-type cubic	5.7	1.0486
Yb_2O_3	C-type cubic	10.8	1.0427
Lu_2O_3	C-type cubic	13.9	1.0390

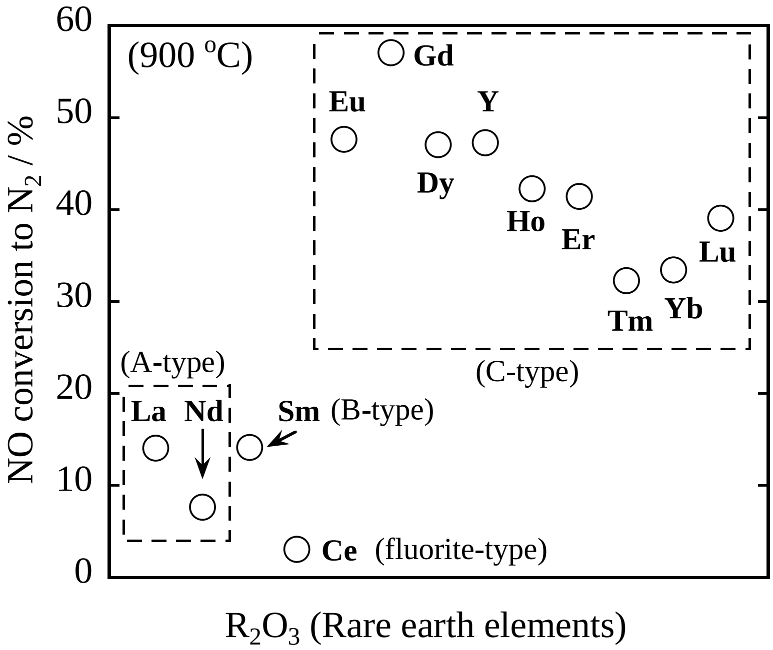

Figure 1.3 Dependence of the rare earth elements on the NO conversion to N_2 on the REOs.

Figure 1.4 shows FT-IR spectra of Er_2O_3 (C-type cubic), Sm_2O_3 (B-type monoclinic), La_2O_3 (A-type hexagonal), and CeO_2 (cubic fluorite-type) obtained after NO adsorption. A peak assigned to nitrosyl $(N–O)^-$ was recognized at 1384 cm^{-1} for all samples [39]. Only on the C-type cubic Er_2O_3, the bands assigned to bidentate (νN=O) nitrate and unidentate carbonate ($\nu_{as}COO^-$) were also observed at 1633 cm^{-1} and 1518 cm^{-1} [40, 41], respectively. The adsorbed carbonate species was probably produced by the carbon dioxide in the atmosphere in the process of the pelletization with KBr. The band intensity of the nitrosyl was increased with decreasing the coordination number of the rare earth ion in the crystal structure in the order of fluorite-type CeO_2 (8 coordination) < A-type La_2O_3 (7 coordination) < B-type Sm_2O_3 (7 and 6 coordination) < C-type Er_2O_3 (6 coordination). This result evidences that the NO adsorption state was significantly affected by the coordination environment of the rare earth ions in the crystal structure: the lower the coordination number becomes, the more NO adsorbs on the surface of the REOs.

Accordingly, loosening of the steric crowding around the rare earth ions facilitates NO adsorption.

To analyze the NO adsorption behavior on the C-type cubic REOs, FT-IR spectra of Eu_2O_3, Gd_2O_3, Dy_2O_3, Y_2O_3, Ho_2O_3, Er_2O_3, Tm_2O_3, Yb_2O_3, and Lu_2O_3 were measured after the NO adsorption as shown in **Figure 1.5**. The spectra are sorted in descending order of the number of basic sites, which was estimated from the CO_2-TPD measurement and is depicted in parentheses. The peaks assigned to nitrosyl $(N–O)^-$ and bidentate nitrate (νN=O) were observed at 1384 cm^{-1} and 1633 cm^{-1} with a broad one corresponding to unidentate carbonate ($\nu_{as}COO^-$) at around 1518 cm^{-1} [39–41]. The peak intensity of the nitrosyl (1384 cm^{-1}) increases with the number of surface basic sites, indicating that the surface basic sites play an important role in the nitrosyl formation on the surface of the C-type cubic REOs.

It was confirmed by the gas analysis after passing through the C-type REOs that a small amount of oxygen desorbed from the oxides when NO adsorbed on the surface of the C-type REOs. In this process, two surface oxide ions desorbed as an oxygen molecule leaving two oxide anion vacancies and four electrons. Some of these electrons are trapped in the oxide anion vacancies to form F and F^+ centers and others are moved to the adsorbed NO to produce nitrosyl (NO^-). Here, the F center is an oxide anion vacancy in which two electrons are trapped and the F^+ center is that trapping one electron, respectively. The formation of the F and F^+ centers was confirmed by the ESR measurement. **Figure 1.6** shows the room temperature ESR spectrum of Y_2O_3 obtained after the NO adsorption. A weak and broad peak appeared between 3450 and 3500 G (Center 1) can be assigned to surface oxide anion vacancy in which an electron or unshared electron pair was trapped [42, 43]. This indicates that some electrons generated by O_2 desorption were trapped in the oxide anion vacancies to form F and F^+ centers.

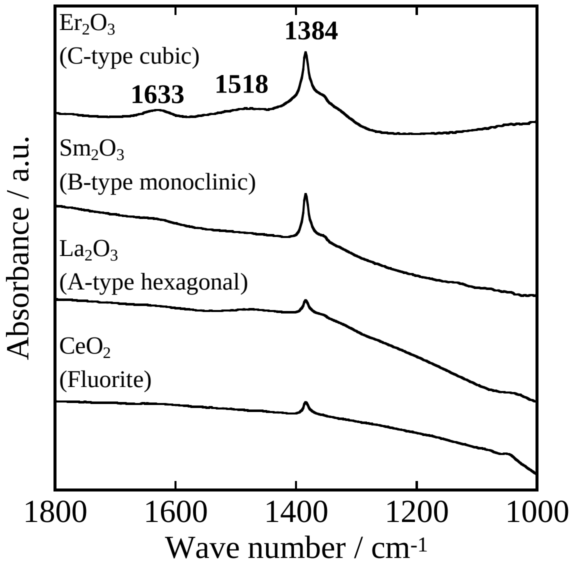

Figure 1.4 FT-IR spectra of Er_2O_3, Sm_2O_3, La_2O_3, and CeO_2 exposed to 1 vol% NO/He for 30 min at room temperature.

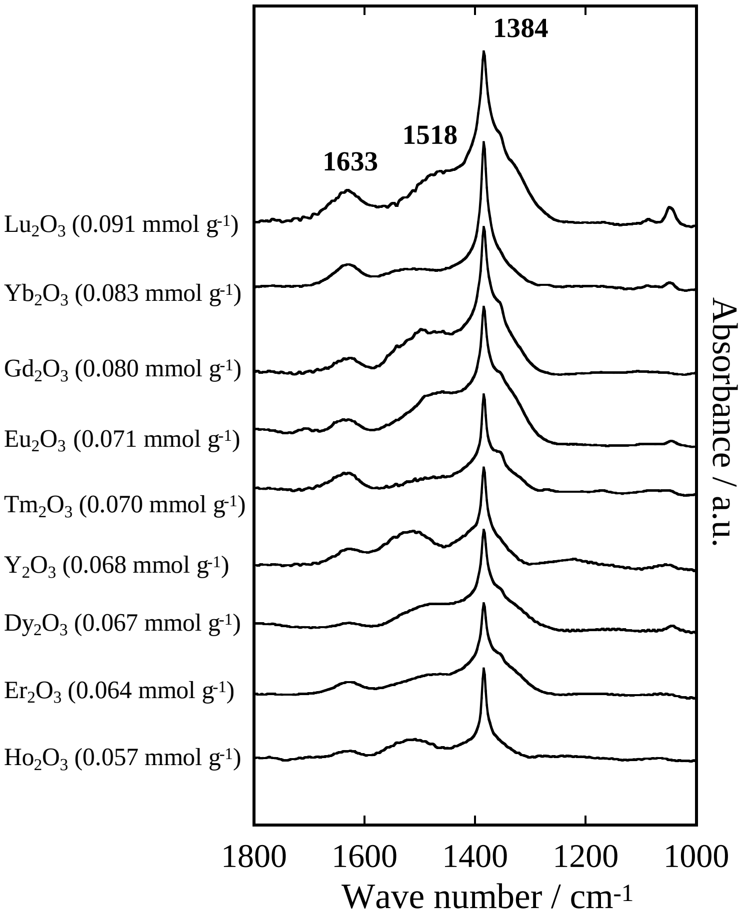

Figure 1.5 FT-IR spectra of C-type cubic REOs (Eu_2O_3, Gd_2O_3, Dy_2O_3, Y_2O_3, Ho_2O_3, Er_2O_3, Tm_2O_3, Yb_2O_3, and Lu_2O_3) exposed to 1 vol% NO/He for 30 min at room temperature.

Therefore, it is reasonable to consider that the adsorbed NO molecules were reduced to nytrosyl by these electrons produced in the O_2 desorption process. Since the amount of F and F^+ centers on oxide surface is generally limited [44], most of the electrons are made available for the formation of nytrosyl. The amount of nytrosyl should increase with the increase in that of the surface oxide anion defect, that is, the basic sites. Actually, as already shown in **Figure 1.5**, the intensity of the nitrosyl at 1384 cm^{-1} correlated with the number of basic sites on the surface of the REOs.

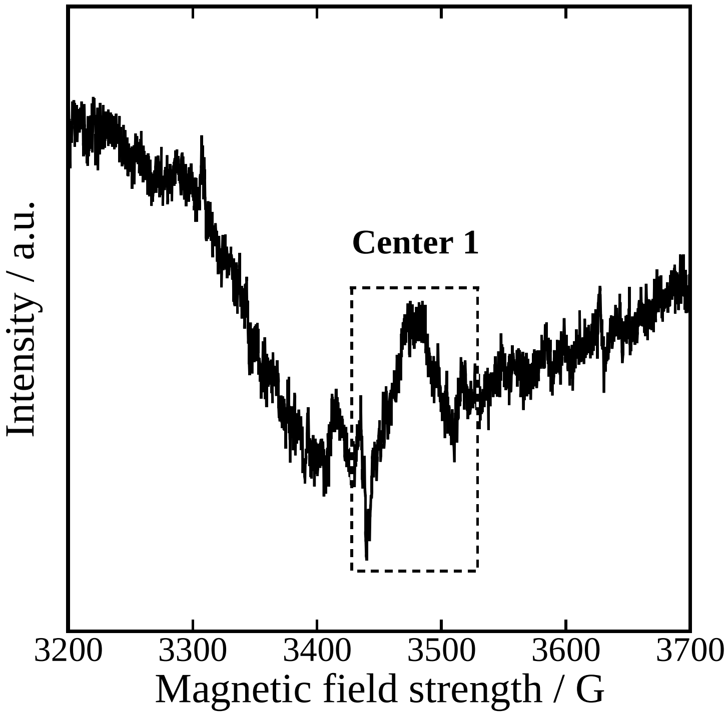

Figure 1.6 Room temperature ESR spectrum of Y_2O_3 after NO adsorption.

The N_2 yield at 900 °C for C-type cubic REOs was plotted in **Figure 1.7** as a function of the number of basic sites. In this figure, the C-type REOs can be classified into two groups based on their lattice parameters. The oxides having a lattice parameter of 1.0597 nm or more were shown in open squares (group 1: □), and those of 1.0486 nm or less were plotted in closed circles (group 2: ●). Er_2O_3 has the intermediate lattice parameter of 1.0545 nm and is expressed in a gray diamond (◆). The oxides belonging to the group 1 showed high N_2 yield more than 40 %, whereas the N_2 yield for the oxides of the group 2 was less than 40 %: high NO decomposition activity was obtained for the oxides with relatively large lattice parameters (1.0597 nm or more). Furthermore, a linear relationship between the N_2 yield and the number of the basic sites was observed both in the groups 1 (□) and 2 (●).

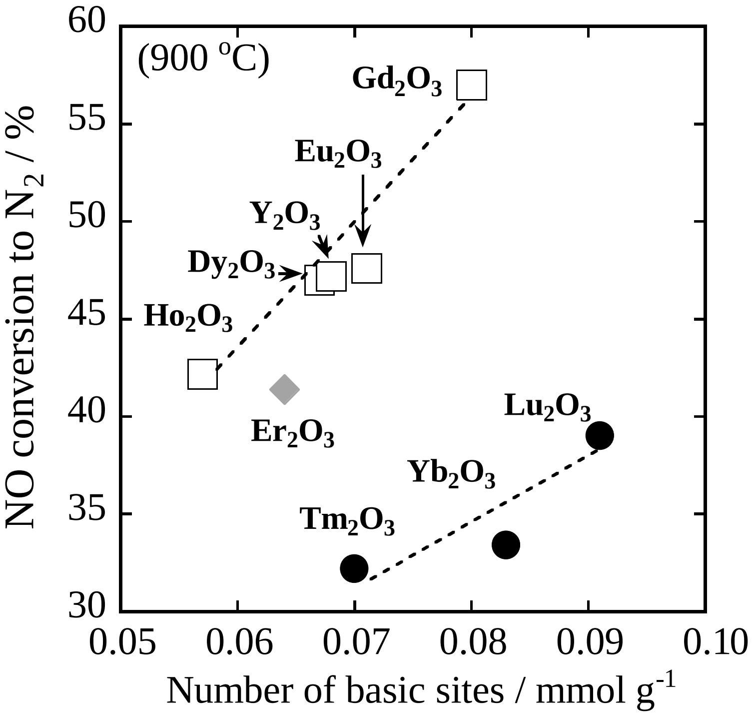

Figure 1.7 Dependence of N_2 yield for C-type cubic REOs on the number of basic sites. The oxides having a lattice parameter of 1.0597 nm or more (group 1) are shown in open squares (□) and those of 1.0486 nm or less (group 2) are plotted in closed circles (●). Er_2O_3, which has an intermediate one of 1.0545 nm, is expressed in a gray diamond (◆).

The microstructure of the C-type cubic REOs was observed by SEM (**Figure 1.8**). The lattice parameters in nanometer scale were depicted in parentheses. Three different of morphologies are observed in SEM images: plate-like for Eu_2O_3, Gd_2O_3, Dy_2O_3, Ho_2O_3, and Y_2O_3, unspecific-shape for Tm_2O_3, Yb_2O_3, and Lu_2O_3, and mixing of plate-like and unspecific-shape for Er_2O_3. **Figure 1.9** shows TEM images of Y_2O_3 (plate-like morphology) and Lu_2O_3 (unspecific-shape). The Lu_2O_3 nanoparticles have an approximately cubic shape with the particle size of several dozen nanometers. In the case of Y_2O_3, on the contrary, the primary particles are significantly agglomerated to form plate-like secondary ones with a side length of a few micrometers. These results suggest that pseudo agglomeration [45] occurs for the REOs synthesized by the calcination of carbonate precursors at a high temperature: the agglomeration structure of the carbonate precursors was preserved after calcination to produce corresponding oxides. Accordingly, the morphology of the REOs highly depends on the microstructure of the carbonate precursors.

Taking into account of the results in **Figs. 1.8 and 1.9**, the plate-like morphology was observed for the oxides with the lattice parameter of 1.0594 nm or more: Eu_2O_3, Gd_2O_3, Dy_2O_3, Ho_2O_3, and Y_2O_3. These oxides were categorized in group 1 and showed relatively high catalytic activities. In contrast, unspecific-shape morphology was observed for Tm_2O_3, Yb_2O_3, and Lu_2O_3 having the lattice parameter of 1.0486 nm or less (group 2), and their NO decomposition activities were relatively low. From the XRD measurements of these REOs, it was confirmed that the plate-like oxides had higher crystallinity than those of the others. Therefore, the morphology and crystallinity of the particles are dominated by the lattice parameter of the REOs, and the oxides of plate-like morphology show high NO decomposition activity. In addition, the catalytic activity increases with increasing the amount of the surface basic sites when the oxides have the same morphology: in the same group. In the case of Er_2O_3, which is a mixture of plate-like and unspecific-shape particles, the catalytic activity falls into an intermediate location between group 1 (plate-like) and group 2 (unspecific-shape), as evidenced in **Fig. 1.7**.

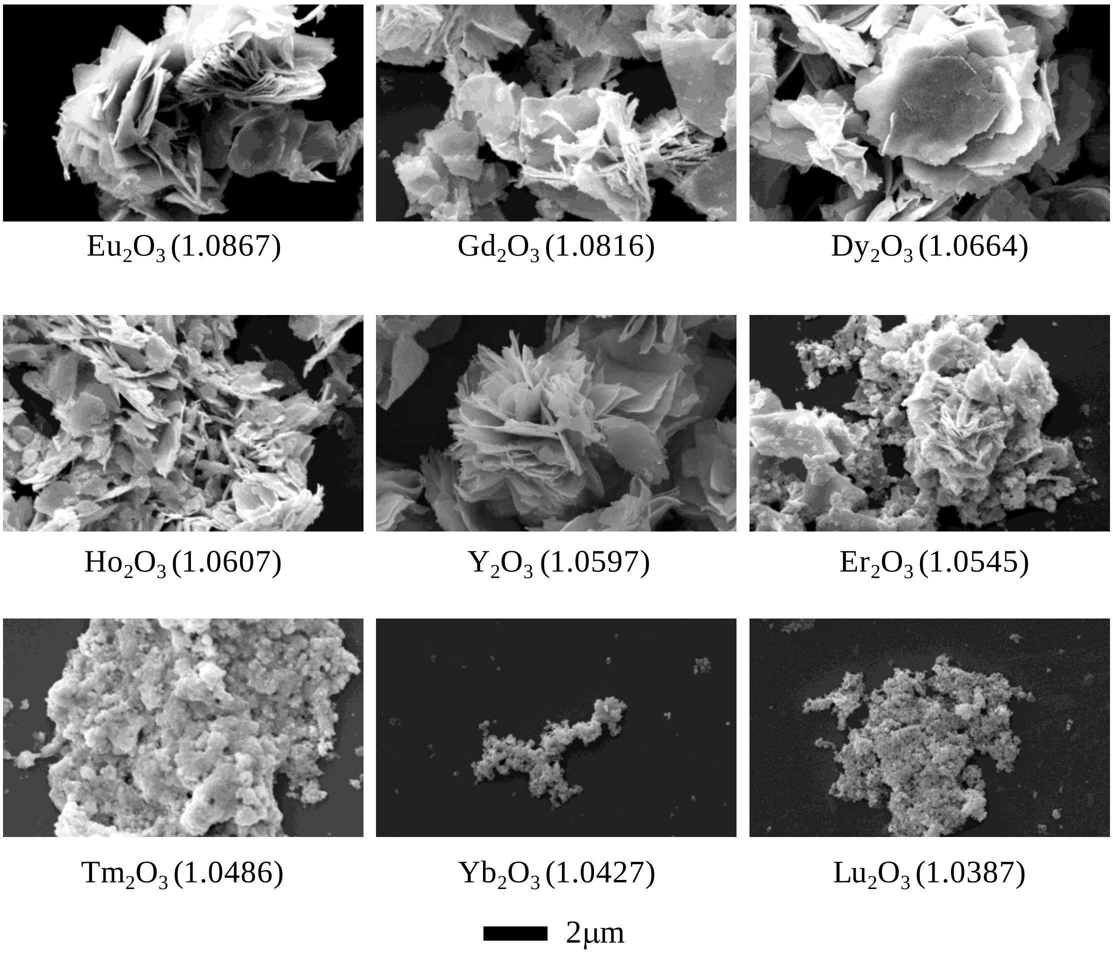
Eu_2O_3 (1.0867)
Gd_2O_3 (1.0816)
Dy_2O_3 (1.0664)
Ho_2O_3 (1.0607)
Y_2O_3 (1.0597)
Er_2O_3 (1.0545)
Tm_2O_3 (1.0486)
Yb_2O_3 (1.0427)
Lu_2O_3 (1.0387)

Figure 1.8 SEM images of C-type cubic REOs (Eu_2O_3, Gd_2O_3, Dy_2O_3, Y_2O_3, Ho_2O_3, Er_2O_3, Tm_2O_3, Yb_2O_3, and Lu_2O_3).

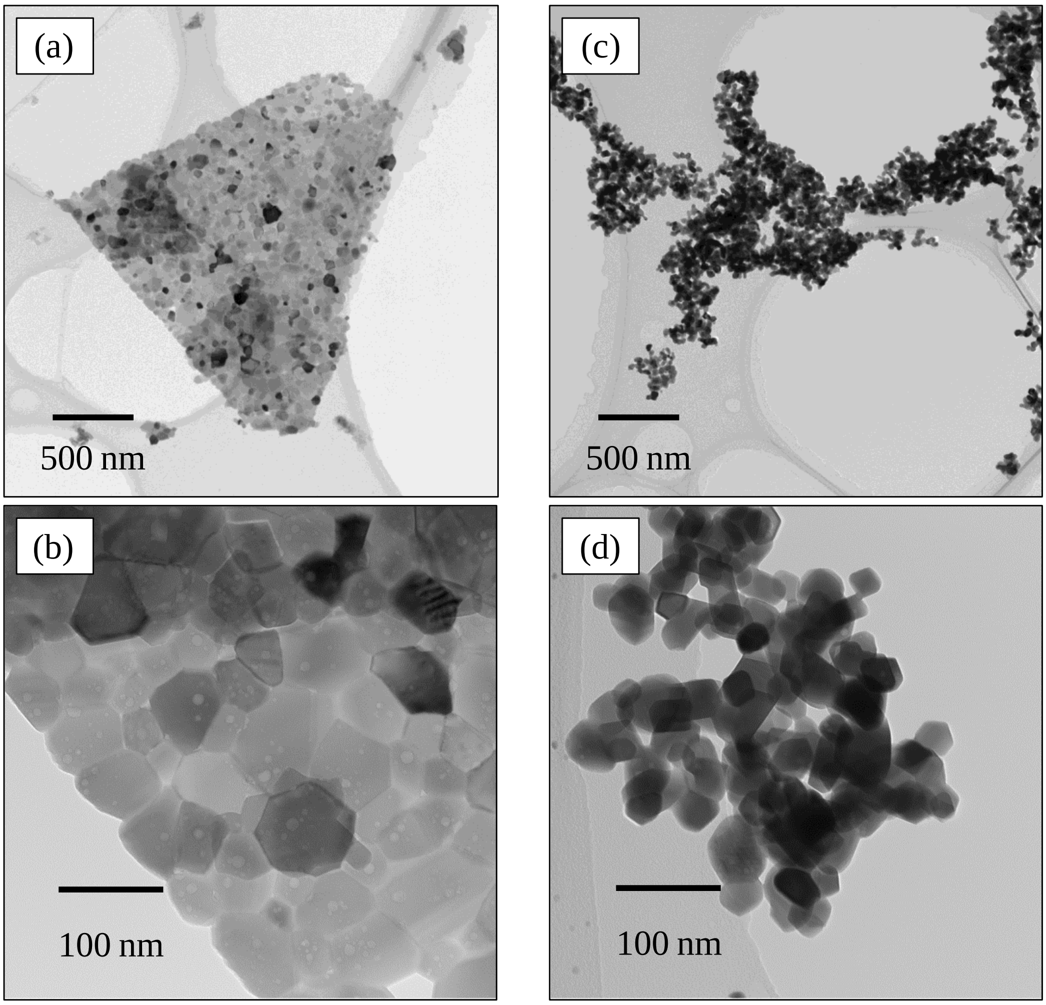

Figure 1.9 TEM images of Y_2O_3 (Direct Mag: (a) 8000×, (b) 50,000×) and Lu_2O_3 (Direct Mag: (c) 8000×, (d) 50,000×).

1.4 Conclusions

In this chapter, structure dependence of the REOs on the NO decomposition activity was discussed from the standpoint of the coordination environment of the rare earth ions. Then, the fundamental factors that contribute to the NO decomposition catalysis, surface basicity, lattice parameter, and morphology of the C-type cubic REOs were characterized and their relationships to the NO decomposition activities were investigated. As a result, the following findings were obtained.

The crystal structure is the most important to promote direct NO decomposition on REOs, because adsorptive capability for NO highly depends on the coordination environment of the rare earth cation in its crystal lattice. Since small coordination number is preferable for NO adsorption, C-type cubic REOs showed higher activity than those of other A- and B-type oxides.

In the series of the C-type cubic REOs, the NO decomposition activity depends on the morphology of the particles correlating with the crystallinity of the REOs. The particle morphology depends on the lattice parameter of the C-type cubic REOs, and the plate-like oxides of high crystallinity show relatively high activities. The pseudo agglomeration should be the reason for the formation of plate-like oxides, and the catalytic activity increases with increasing the amount of the surface basic sites when the oxides have the same morphology. Therefore, the fundamental four factors for REOs to exhibit high direct NO decomposition activity are crystal structure, lattice parameter, particle morphology, and the number of basic sites, and the activity was determined by the combination of them.

Chapter 2 Effects of the Introduction of Alkaline Earth Metal and Terbium Ions on the NO Decomposition Activity of C-type Cubic Y_2O_3

2.1 Introduction

In this chapter, Y_2O_3–AO (A : Ba, Sr, and Ca) solid solutions were synthesized to investigate the effects of the introduction of alkaline earth metal ions into the C-type cubic Y_2O_3 on the NO decomposition activity. Partial substitution of trivalent Y^{3+} with divalent alkaline earth metal ion generates oxide anion vacancies by charge compensation, so that the amount of active sites for NO adsorption and decomposition is increased. In addition, oxides of alkaline earth metals are typical basic oxides, and, in particular, barium oxide is a well-known NO_x storage component used in the NSR catalyst [46, 47]. A number of experimental and theoretical studies suggest that NO_x is generally adsorbed onto the Ba^{2+} sites as nitrites or nitrates [48–50]. Accordingly, the effects of the introduction of alkaline earth metal ions on the NO decomposition activity should be evaluated from the aspect of surface basicity and NO adsorption state on the basic site.

In addition to the above considerations, in this chapter, the effects of $Tb^{3+/4+}$ doping on the catalytic activity was also investigated in the Y_2O_3–Tb_4O_7 system. The presence of metal ions, which can take multiple valence state, in the lattice is effective to accelerate desorption of oxygen from the catalyst surface using its redox property, and, as a result, the NO decomposition activity is increased [32]. Therefore, the relationship between NO decomposition activity and O_2 desorption behavior was investigated on the Y_2O_3-Tb_4O_7 solid solutions, in which the reduction of Tb^{4+} to Tb^{3+} could take place smoothly to facilitate O_2 desorption. Finally, the effects of double doping of Ba^{2+} and $Tb^{3+/4+}$ on the NO decomposition activity of Y_2O_3 were investigated.

2.2 Experimental Procedure

The C-type cubic $(Y_{0.99}A_{0.01})_2O_{2.99}$ (A: Ba, Sr, and Ca), $(Y_{1-x}Tb_x)_2O_{3+\delta}$ ($0 \leq x \leq 0.30$), and $(Y_{0.69}Tb_{0.30}Ba_{0.01})_2O_{2.99+\delta}$ were synthesized by a carbonate co-precipitation method. A stoichiometric mixture of 1.0 mol dm^{-3} $Y(NO_3)_3$, 0.1 mol dm^{-3} $A(NO_3)_2$ (A: Ba, Sr, and Ca), and 0.1 mol dm^{-3} $Tb(NO_3)_3$ aqueous solutions was added to a 1.0 mol dm^{-3} ammonium carbonate solution with stirring, and the total amount of the cations was adjusted to be 10 mmol. The pH of the mixture was adjusted to 10 by dropwise addition of ammonia solution. After stirring for 6 h, the resulting precipitate was collected by filtration, washed several times with deionized water, and then dried at 80 °C for 6 h. The powder was then ground in an agate mortar and finally calicined at 900 °C in air for 6 h.

The catalysts were characterized by X-ray fluorescence (XRF) analysis and X-ray powder diffraction (XRD). NO adsorption state and the number of basic sites of the catalysts were examined using FT-IR and CO_2-TPD measurements, respectively. The NO decomposition activity was tested by the similar procedure described in Chapter 1-2 (for details to p.13). The concentrations of NO_2 and N_2O in the effluent gas were assessed *via* a gas chromatograph-mass spectrometer (GC-MS; Shimadzu, GCMS-QP2010 Plus).

O_2-TPD measurements were conducted after adsorption of O_2 at 600 °C for 1 h. After heating the catalyst in a flow of He (30 cm^3 min^{-1}) at 600 °C for 30 min, the catalyst was exposed to O_2 (1 atm) at the same temperature for 1 h, and then cooled to 50 °C. After evacuation at 50 °C for 30 min, the catalyst was heated under a flow of He at a heating rate of 10 °C min^{-1} and the desorbed gas was monitored using the BELCAT-B apparatus. X-ray photoelectron spectroscopy (XPS; ULVAC 5500MT) was performed at room temperature using Mg-Kα radiation (1253.6 eV). The effect of charging on the binding energies was corrected with respect to the C1s peak at 284.6 eV.

2.3 Results and Discussion

$(Y_{0.99}A_{0.01})_2O_{2.99}$ (A: Ba, Sr, and Ca) catalysts were synthesized with the molar fraction of the alkaline earth metal ions fixed at 1 mol%, because the ionic radius of these ions are significantly larger than that of Y^{3+} [51] and the introduction of an excessive amount of these ions induced formation of impurities. Actually, the addition of Ba^{2+} in concentrations more than 1 mol% to Y_2O_3 induced the formation of $BaCO_3$ as a secondary impurity phase.

Figure 2.1 shows XRD patterns of the $(Y_{0.99}A_{0.01})_2O_{2.99}$ (A: Ba, Sr, and Ca) catalysts with that of Y_2O_3. All the diffraction patterns were assigned to typical C-type cubic structure, and no crystalline impurities were observed. **Figure 2.2** depicts the dependence of the lattice parameters of $(Y_{0.99}A_{0.01})_2O_{2.99}$ (A: Ba, Sr, and Ca) estimated from the XRD patterns on the ionic radius of the dopant for 6 coordination (Ba^{2+}: 0.149 nm, Sr^{2+}: 0.132 nm, and Ca: 0.114 nm [51]). The lattice parameter of Y_2O_3 was also manifested in a closed circle as a standard. The lattice parameter proportionally increased with increasing the ionic radius of the dopant, indicating the formation of the solid solutions in a single phase of the C-type cubic structure.

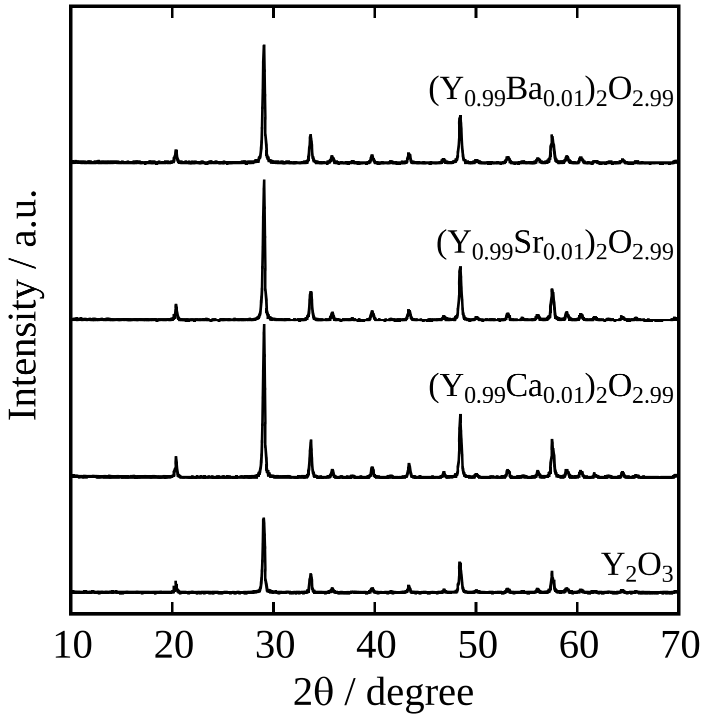

Figure 2.1 XRD patterns of $(Y_{0.99}A_{0.01})_2O_{2.99}$ (A: Ba, Sr, and Ca) and Y_2O_3.

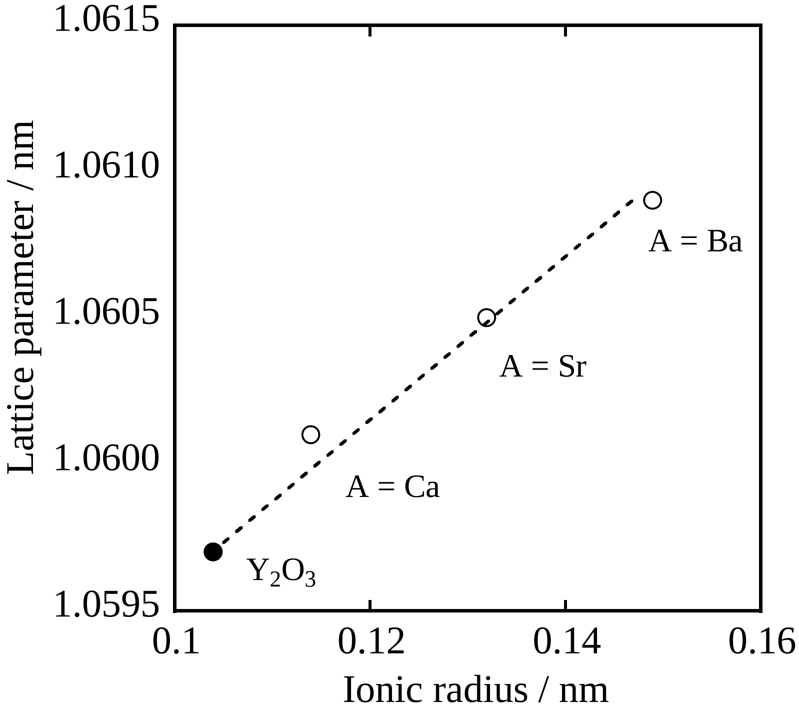

Figure 2.2 Dependence of the lattice parameters of $(Y_{0.99}A_{0.01})_2O_{2.99}$ (A: Ba, Sr, and Ca) (○) on the ionic radius of the dopant. The lattice parameter of Y_2O_3 was also plotted as a reference (●).

Figure 2.3 shows the temperature dependence of NO conversion to N_2 for $(Y_{0.99}A_{0.01})_2O_{2.99}$ (A: Ba, Sr, and Ca) and Y_2O_3. The NO decomposition activity appeared at 650 °C and above and the N_2 yield increased monotonically with increasing the reaction temperature. The formation of N_2O was not detected between 400 to 900 °C. The NO decomposition activity was enhanced by the introduction of alkaline earth metal ions into the Y_2O_3 lattice, among which the Ba^{2+} and Sr^{2+} doping are significantly effective to enhance the catalytic activity. As a result, the highest NO decomposition activity was obtained for $(Y_{0.99}Ba_{0.01})_2O_{2.99}$, where the N_2 yield obtained over this catalyst was 76 % at 900 °C.

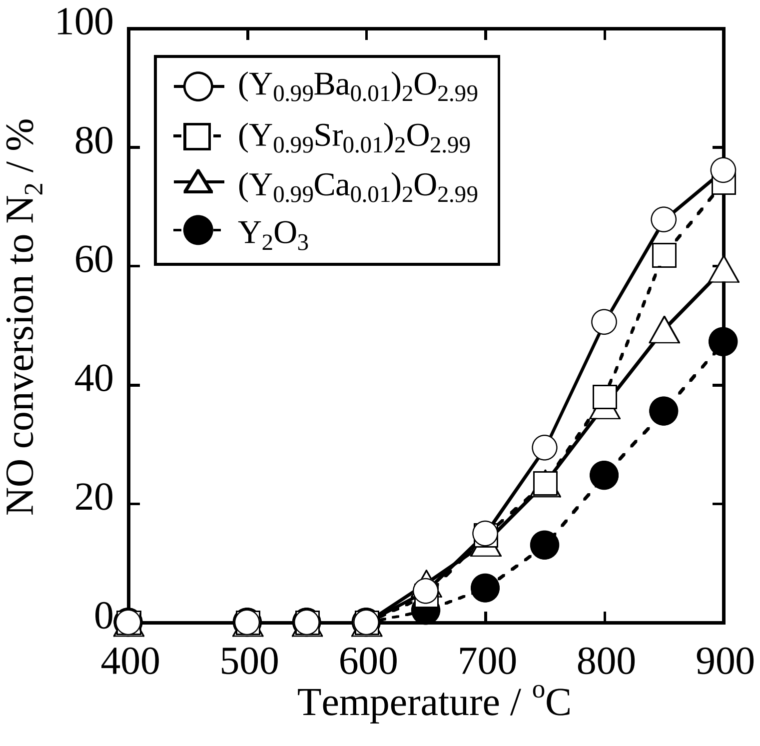

Figure 2.3 Temperature dependence of NO conversion to N_2 over $(Y_{0.99}A_{0.01})_2O_{2.99}$ (A: Ba, Sr, and Ca) and Y_2O_3 (NO: 1 vol%; He balance; *W/F* = 3.0 g s cm^{-3}).

The CO_2-TPD profiles for $(Y_{0.99}A_{0.01})_2O_{2.99}$ (A: Ba, Sr, and Ca) and Y_2O_3 are shown in **Figure 2.4**. The amounts of desorbed CO_2, *i.e.*, the number of basic sites, estimated from the desorption peak areas are depicted in parentheses. The CO_2 desorption peaks were observed in two temperature ranges for all samples: less than 250 °C and between 250 to 600 °C. The former and the latter were attributed to the desorption of chemisorbed CO_2 and structural carbonate, respectively [52]. When alkaline earth cations were dissolved in the Y_2O_3 lattice, the amount of the CO_2 desorption increased. In particular, the desorption peak intensity around 350 °C was significantly increased, indicating that the partial substitution of Y^{3+} with divalent Ba^{2+}, Sr^{2+}, or Ca^{2+} was effective to increase the number of strong basic sites.

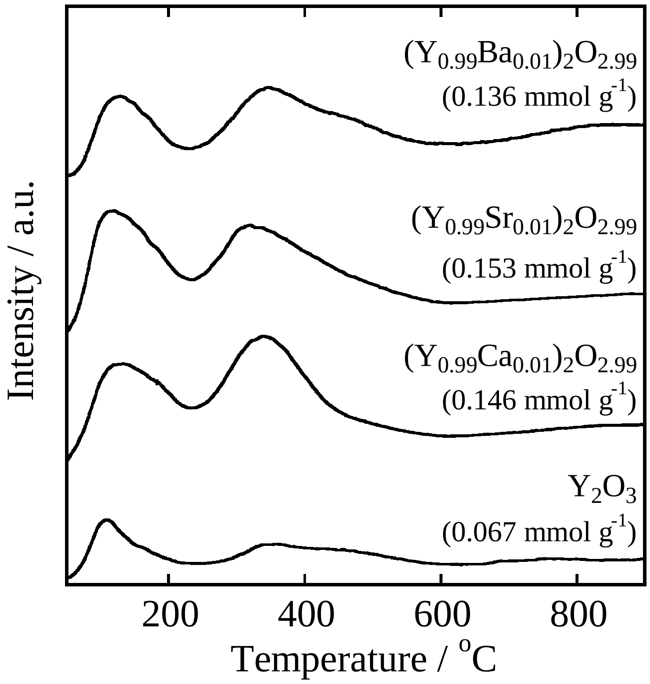

Figure 2.4 CO_2-TPD profiles for $(Y_{0.99}A_{0.01})_2O_{2.99}$ (A : Ba, Sr, and Ca).

In order to identify the NO adsorption state, FT-IR measurements were carried out on $(Y_{0.99}A_{0.01})_2O_{2.99}$ (A: Ba, Sr, and Ca). **Figure 2.5** shows FT-IR spectra of $(Y_{0.99}A_{0.01})_2O_{2.99}$ (A: Ba, Sr, and Ca) obtained after NO adsorption. Two broad absorption peaks at around 1384 cm^{-1} and 1518 cm^{-1} are corresponding to unidentate carbonate (ν_{as}COO^{-}) [39–41], which was produced during the process of KBr pellet preparation. A sharp peak assigned to nitrosyl (N−O^{-}) was observed at 1384 cm^{-1} [39], and the bands corresponding to bidentate and unidentate nitrate were recognized at 1633 and 1271 cm^{-1} [40], respectively. In particular, the peak assigned to unidentate nitrate (1271 cm^{-1}) appeared when divalent cations were introduced into the Y_2O_3 lattice, and the intensity of this peak increased along with the decrease of nitrosyl at 1384 cm^{-1}, suggesting that adsorbed nitrosyl was oxidized to unidentate nitrate on the catalyst surface. Since the NO adsorption was carried out in a flow of 1.0 vol% NO/He, it is reasonable to consider that the nitrosyl was oxidized by surface oxide anions. The oxidation of nitrosyl brings about the formation of new oxide anion vacancies and rare earth ions of low coordination numbers on the catalyst surface to increase the catalytic activity. As seen in Fig. 2.5, the formation of these surface defects is favorable for $(Y_{0.99}Ba_{0.01})_2O_{2.99}$ and $(Y_{0.99}Sr_{0.01})_2O_{2.99}$,

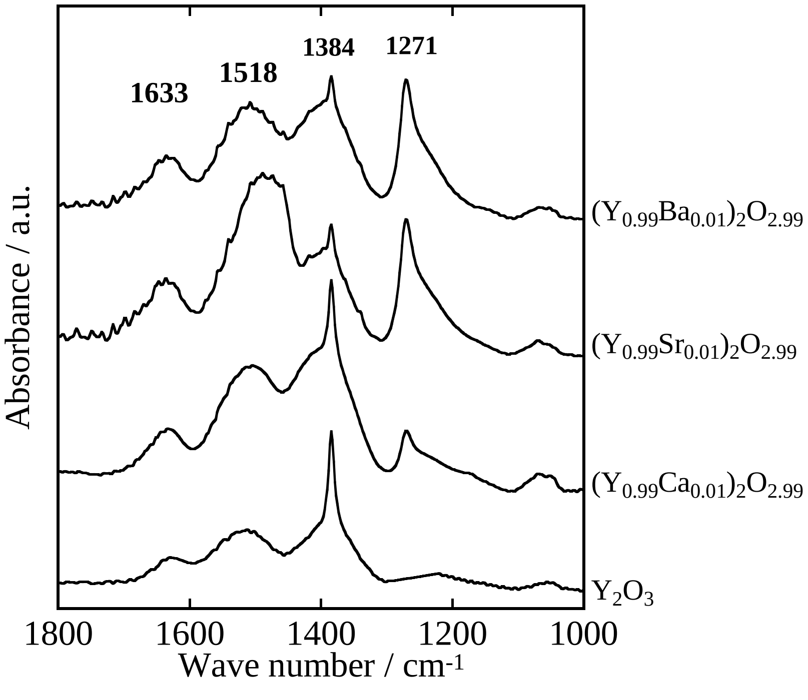

Figure 2.5 FT-IR spectra for $(Y_{0.99}A_{0.01})_2O_{2.99}$ (A : Ba, Sr, and Ca) exposed to 1 vol% NO/He for 30 min at room temperature.

because unidentate nitrate became dominant species adsorbed on these catalysts. As a result, the relatively high NO decomposition activities were observed in Fig. 2.3 for $(Y_{0.99}Ba_{0.01})_2O_{2.99}$ and $(Y_{0.99}Sr_{0.01})_2O_{2.99}$.

Subsequently, the effects of $Tb^{3+/4+}$ doping on the NO decomposition activity were examined. **Figure 2.6** shows XRD patterns of the $(Y_{1-x}Tb_x)_2O_{3+\delta}$ $(0 \leq x \leq 0.30)$ catalysts. All the diffraction patterns can be assigned to typical C-type cubic rare earth oxide with a single phase structure, and no crystalline impurities were detected. In the case of $(Y_{0.70}Tb_{0.30})_2O_{3+\delta}$, on the other hand, some small peaks almost disappeared, because the introduction of some tetravalent terbium ions decreased the oxide anion vacancies in the C-type cubic lattice, and, as a result, the crystal structure was gradually transformed to the oxygen-deficient fluorite-related structure. However, the fundamental lattice structure remains essentially unchanged.

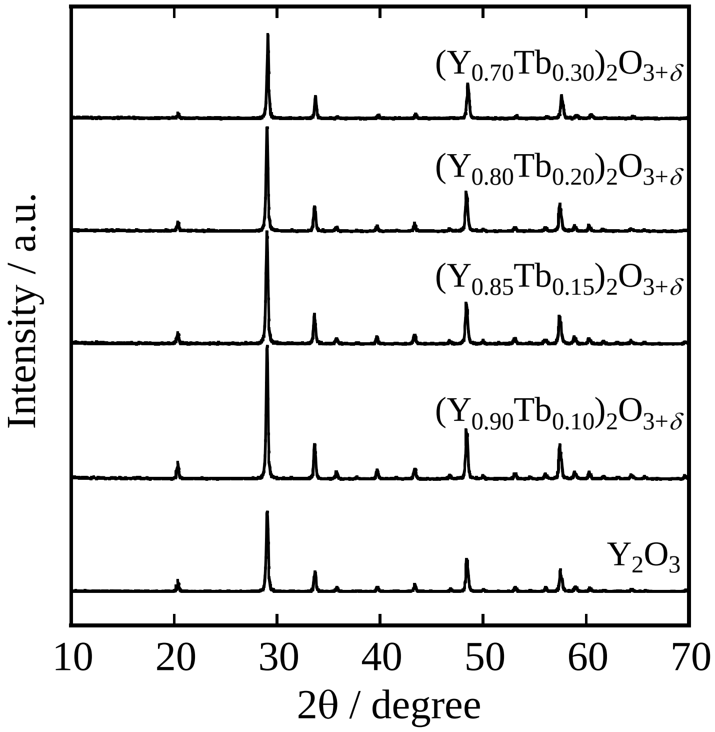

Figure 2.6 XRD patterns of $(Y_{1-x}Tb_x)_2O_{3+\delta}$ $(0 \leq x \leq 0.30)$.

Figure 2.7 shows the dependence of NO conversion to N_2 at 900 °C on the $Tb^{3+/4+}$ concentration in the $(Y_{1-x}Tb_x)_2O_{3+\delta}$ catalysts (**Figure 2.7 (a)**) and the temperature dependence of the N_2 yield when using $(Y_{0.80}Tb_{0.20})_2O_{3+\delta}$ (**Figure 2.7 (b)**). As seen in **Figure 2.7**, the NO decomposition activity was enhanced by the introduction of $Tb^{3+/4+}$. The highest catalytic activity was obtained for $(Y_{0.80}Tb_{0.20})_2O_{3+\delta}$, on which the N_2 yield was 64 % at 900 °C. The N_2 formation was detected at 650 °C and above and the yield increased monotonically with increasing the reaction temperature as was the case in $(Y_{0.99}A_{0.01})_2O_{2.99}$ (A: Ba, Sr, and Ca). Although a small amount of N_2O was generated between 500 and 750 °C, neither N_2O nor NO_2 were detected above 800 °C.

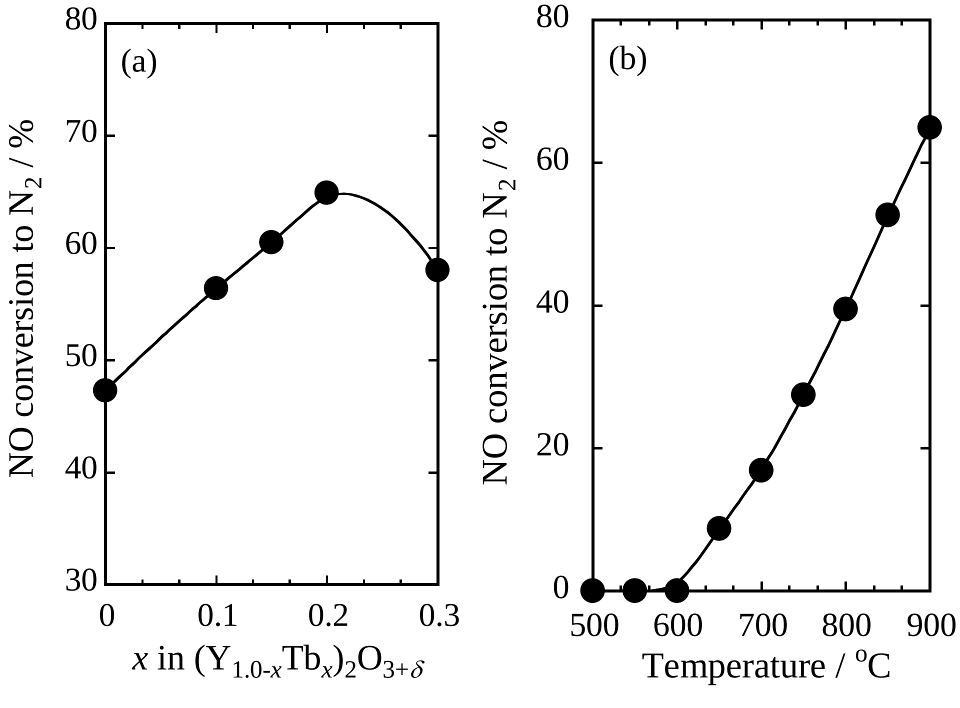

Figure 2.7 Variations in NO conversion to N_2 at 900 °C as a function of (a) the terbium concentration in $(Y_{1-x}Tb_x)_2O_{3+\delta}$ ($0 \le x \le 0.30$) and (b) temperature (over the $(Y_{0.80}Tb_{0.20})_2O_{3+\delta}$ catalyst).

The dependence of the lattice constant on the concentration of $Tb^{3+/4+}$ in $(Y_{1-x}Tb_x)_2O_{3+\delta}$ ($0 \leq x \leq 0.30$) is shown in **Figure 2.8**. Comparison of the lattice constant before and after the catalytic performance test for NO decomposition revealed lattice expansion after the reaction. This is probably due to the reduction of smaller Tb^{4+} to larger Tb^{3+} during NO decomposition.

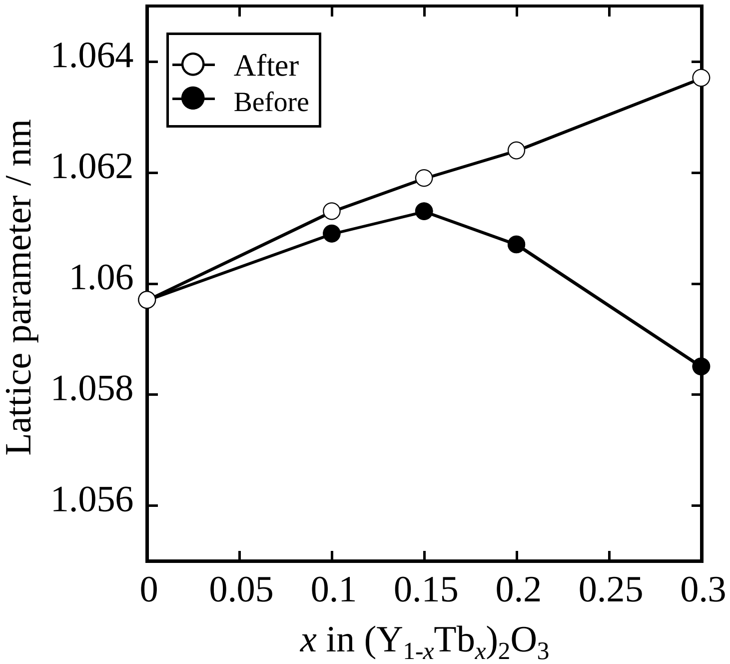

Figure 2.8 Dependence of the lattice parameter on the concentration of $Tb^{3+/4+}$ in $(Y_{1-x}Tb_x)_2O_{3+\delta}$ ($0 \leq x \leq 0.30$) before (●) and after (○) the catalytic test for NO decomposition.

Figure 2.9 presents O_2-TPD profiles for $(Y_{1-x}Tb_x)_2O_{3+\delta}$, where O_2 was adsorbed at 600 °C. The amounts of desorbed O_2 estimated from the peak areas are depicted in parentheses. Sharp O_2 desorption peaks were observed in the range of temperature from 300 to 500 °C, which can be assigned to desorption of chemisorbed oxygen from the catalyst surface, because O_2 adsorption at 600 °C is dissociative [40]. The amount of O_2 desorbed increased in proportion with increasing $Tb^{3+/4+}$ content (x) in $(Y_{1-x}Tb_x)_2O_{3+\delta}$. The O_2 desorption peak temperature is seen to gradually decrease with increasing amounts of $Tb^{3+/4+}$ until it reaches a minimum at x = 0.15, indicating that the presence of $Tb^{3+/4+}$ weakens the bond strength between the catalyst surface and adsorbed oxygen. However, it turned to shift to the higher temperature side at x = 0.20 and higher, indicating that an excessive amount of $Tb^{3+/4+}$ is unfavorable, since the amount of strongly adsorbed oxygen was increased.

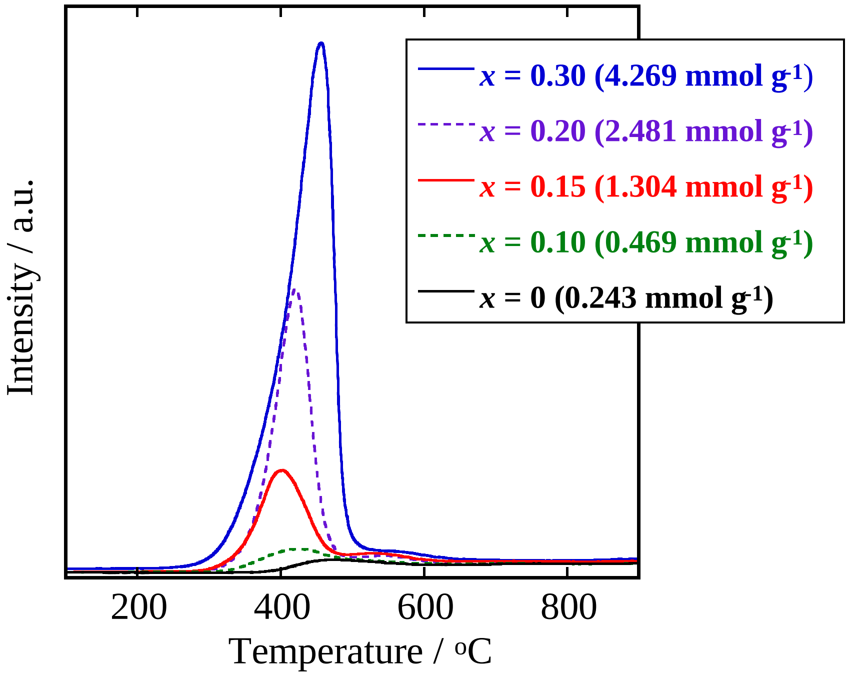

Figure 2.9 O_2-TPD profiles for $(Y_{1-x}Tb_x)_2O_{3+\delta}$ ($0 \leq x \leq 0.30$).

The CO_2-TPD and O_2-TPD profiles for $(Y_{0.69}Tb_{0.30}Ba_{0.01})_2O_{2.99+\delta}$, $(Y_{0.99}Ba_{0.01})_2O_{2.99}$, $(Y_{0.70}Tb_{0.30})_2O_{3+\delta}$, and Y_2O_3 are presented in **Figures 2.10** and **2.11**, respectively, where the peak intensities of the O_2 desorption of Y_2O_3 and $(Y_{0.99}Ba_{0.01})_2O_{2.99}$ are multiplied by 20. The amounts of desorbed CO_2 and O_2 estimated from the peak areas were depicted in parentheses in the figures. From the results of CO_2-TPD, it is found that $(Y_{0.69}Tb_{0.30}Ba_{0.01})_2O_{2.99+\delta}$ and $(Y_{0.99}Ba_{0.01})_2O_{2.99}$ have a large number of strong basic sites. In the O_2-TPD profiles, the O_2 desorption peaks were observed in two temperature regions. Relatively strong and sharp desorption peaks were detected below 600 °C, while small and broad ones are observed above 600 °C. The former and the latter peaks correspond to the desorption of chemisorbed oxygen and lattice oxygen, respectively. In this regard, the presence of $Tb^{3+/4+}$ ions caused a shift of both desorption peaks to the lower temperature side, indicating that the $Tb^{3+/4+}$ doping was effective to enhance the O_2 desorption not only from the surface but also from the bulk.

Figure 2.12 depicts FT-IR spectra for $(Y_{0.69}Tb_{0.30}Ba_{0.01})_2O_{2.99+\delta}$, $(Y_{0.99}Ba_{0.01})_2O_{2.99}$, $(Y_{0.70}Tb_{0.30})_2O_{3+\delta}$, and Y_2O_3 obtained after NO adsorption. The spectrum shape for $(Y_{0.69}Tb_{0.30}Ba_{0.01})_2O_{2.99+\delta}$ was almost the same with that for $(Y_{0.99}Ba_{0.01})_2O_{2.99}$, and the formation of unidentate nitrate resulting from the oxidation of nitrosyl was recognized. XPS spectra of $(Y_{0.69}Tb_{0.30}Ba_{0.01})_2O_{2.99+\delta}$ before and after the catalytic performance test were measured as depicted in **Figure 2.13**. Although the Y_{3d} and the Tb_{4d} core levels are overlapped, the binding energies of $Y^{3+}3d_{5/2}$ and $Y^{3+}3d_{3/2}$ are located at 156.0 and 157.8 eV, with those of $Tb^{3+}{}_{4d}$ at 147.9 and 149.4 eV and $Tb^{4+}{}_{4d}$ at 147.9 and 157.3 eV [53–56]. As can be noticed from this figure, the terbium ion is present in both 3+ and 4+ oxidation states and the binding energy around 158 eV significantly decreased after the catalytic performance test, while those around 148 eV increased. This indicates that some terbium ions are reduced from 4+ to 3+ oxidation states.

As evidenced in the above discussions, the doping effects of both Ba^{2+} and $Tb^{3+/4+}$ are involved in the $(Y_{0.69}Tb_{0.30}Ba_{0.01})_2O_{2.99+\delta}$ catalyst, and, as a result, the significantly high NO decomposition activity (100% decomposition) can be achieved.

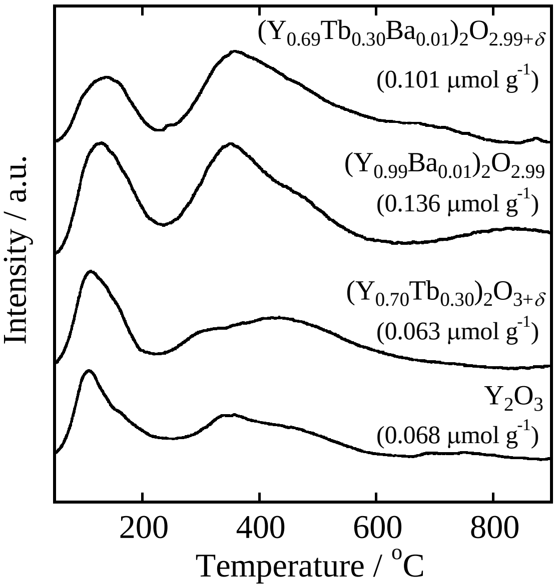

Figure 2.10 CO_2-TPD profiles for $(Y_{0.69}Tb_{0.30}Ba_{0.01})_2O_{2.99+\delta}$, $(Y_{0.99}Ba_{0.01})_2O_{2.99}$, $(Y_{0.70}Tb_{0.30})_2O_{3+\delta}$, and Y_2O_3.

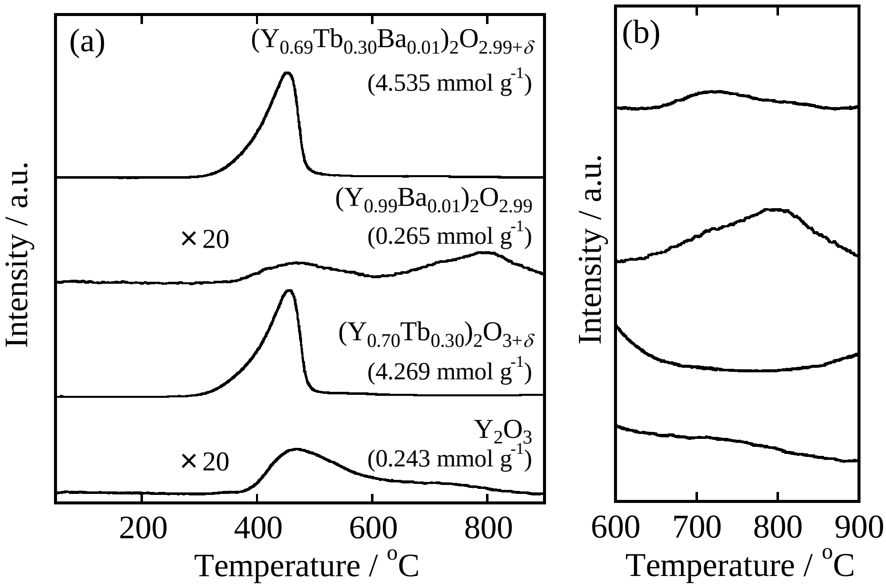

Figure 2.11 O_2-TPD profiles for $(Y_{0.69}Tb_{0.30}Ba_{0.01})_2O_{2.99+\delta}$, $(Y_{0.99}Ba_{0.01})_2O_{2.99}$, $(Y_{0.70}Tb_{0.30})_2O_{3+\delta}$, and Y_2O_3 in the temperature range from 50 to 900 °C (a) and 600 to 900 °C (b).

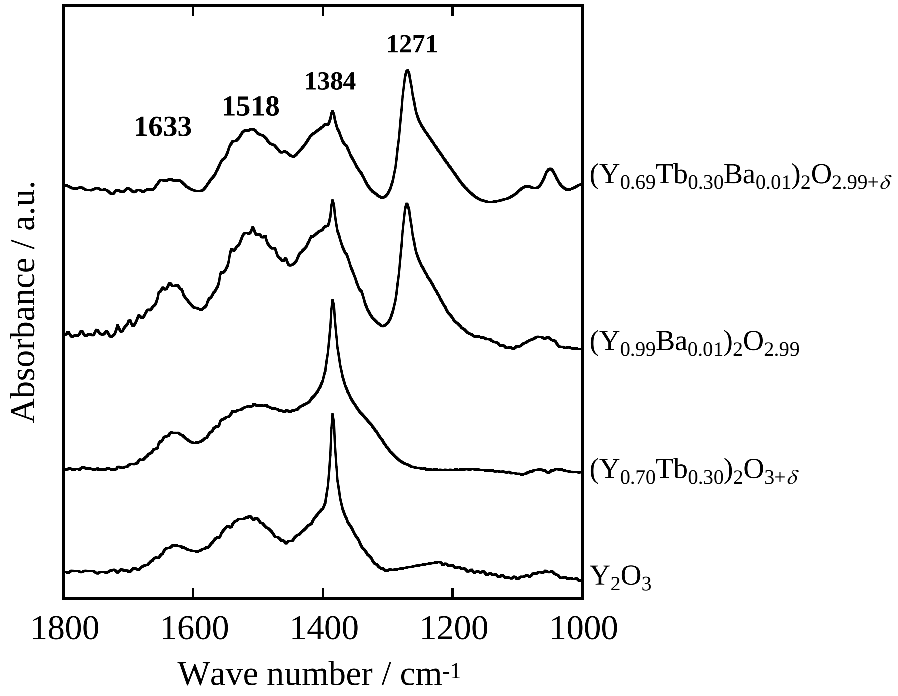

Figure 2.12 FT-IR spectra of $(Y_{0.69}Tb_{0.30}Ba_{0.01})_2O_{2.99+\delta}$, $(Y_{0.99}Ba_{0.01})_2O_{2.99}$, $(Y_{0.70}Tb_{0.30})_2O_{3+\delta}$, and Y_2O_3 exposed to 1 vol% NO/He for 30min at room temperature.

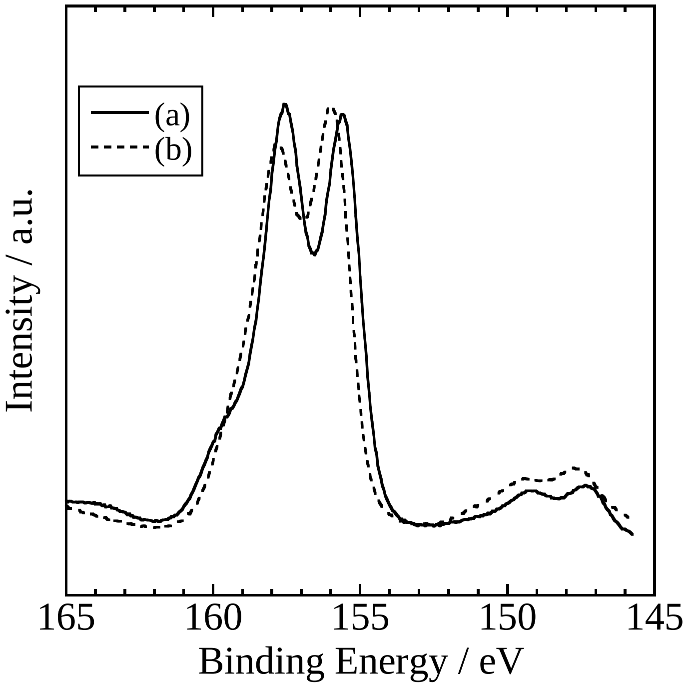

Figure 2.13 XPS spectra for $(Y_{0.69}Tb_{0.30}Ba_{0.01})_2O_{2.99+\delta}$ before (a) and after (b) the catalytic test for NO decomposition.

2.4 Conclusions

The partial substitution of trivalent Y^{3+} ions in C-type cubic Y_2O_3 with divalent cations (Ba^{2+}, Sr^{2+}, and Ca^{2+}) produces oxide anion vacancies in the lattice by charge compensation. The presence of these alkaline earth ions in the lattice induced the oxidation of nitrosyl to unidentate nitrate using surface oxide anions, and consequently, additional oxide anion vacancies were formed on the catalyst surface in this process. Furthermore, the doping of alkaline earth ions increased the number of strong basic sites on the catalyst surface. NO adsorption on the surface of the catalyst is facilitated by these modifications, elucidating that the effects of alkaline earth metal ion are significant.

In contrast, the $Tb^{3+/4+}$ introduction is effective to facilitate O_2 desorption from the catalyst surface, leading to the regeneration of active sites for NO decomposition. Furthermore, the doping effects of both Ba^{2+} and $Tb^{3+/4+}$ are involved in the $(Y_{0.69}Tb_{0.30}Ba_{0.01})_2O_{2.99+\delta}$ catalyst, and, as a result, the significantly high NO decomposition activity (100% decomposition) can be realized.

Chapter 3 Mechanism for Direct NO decomposition over the Catalysts Based on C-type cubic Y_2O_3

3.1 Introduction

As described in **Chapters 1** and **2**, room temperature FT-IR studies confirmed that gaseous NO adsorbs on the catalysts to form nitrosyl and unidentate nitrate on the surface. However, the NO adsorption state on the catalysts in a high temperature region has not been analyzed in detail, so the mechanism of NO decomposition still remains to be clarified.

In this chapter, therefore, the effect of high temperature heating on the FT-IR bands was examined for $(Y_{0.69}Tb_{0.30}Ba_{0.01})_2O_{2.99+\delta}$. Furthermore, the NO adsorption state was also investigated using the TPD measurement. Finally, a mechanism for direct NO decomposition over the REOs-based catalysts is proposed.

3.2 Experimental Procedure

The FT-IR measurements were performed with an FT-IR spectrophotometer (Bruker Optics, Tensor 27) in a dry atmosphere at room temperature (for details see p.12). *In-situ* FT-IR spectroscopy experiments were performed in the diffuse reflectance (DRIFT) mode using a spectrometer (Shimadzu, Prestige-21) with a heat chamber type attachment (S.T. Japan, HC900) in a flow of 1.0 vol% NO and He (balance) at 700 and 800 °C at a rate of 10 $cm^3 min^{-1}$ over 0.1 g of catalyst.

In the NO_x-TPD measurement, the catalyst was heated in a flow of 1 vol% NO/He (30 $cm^3 min^{-1}$) at 600 °C for 30 min, and then cooled to 50 °C. After evacuation at 50 °C for 15 min, the catalyst was heated under a flow of He at a heating rate of 5 °C min^{-1}. The gas composition desorbed from the samples was analyzed using GC-MS (Shimadzu, GCMS-QP2010 Plus).

3.3 Results and Discussion

The effect of high temperature heating on the FT-IR bands was examined for $(Y_{0.69}Tb_{0.30}Ba_{0.01})_2O_{2.99+\delta}$. The catalyst was heated at 200, 400, and 900 °C in a flow of He after NO adsorption. **Figure 3.1** shows that the band intensity of unidentate nitrate at 1271 cm^{-1} decreased with increasing temperature, and this band disappeared at 900 °C. In contrast, the band intensity of nitrosyl at 1384 cm^{-1} was significantly increased by heating at 400 °C, which suggests that the adsorbed unidentate nitrate was transformed to nitrosyl by this heating. This consideration is supported by the results of *in-situ* DRIFT-IR measurement shown in **Figure 3.2**. Drastic change in the base line is attributed to black-body radiation. The DRIFT-IR spectra obtained in a flow of 1 vol% NO/He at 700 and 800 °C have a main band corresponding to adsorbed nitrosyl at 1360 cm^{-1}, and a nominal peak of unidentate nitrate was detected at 1288 cm^{-1}.

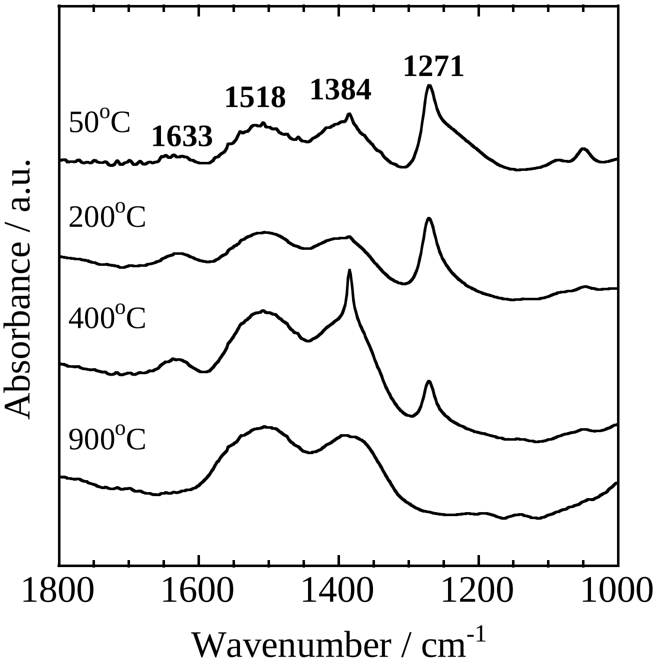

Figure 3.1 (a) FT-IR spectra for $(Y_{0.69}Tb_{0.30}Ba_{0.01})_2O_{2.99+\delta}$ exposed to 1 vol% NO/He for 30 min at 600 °C and subsequently cooled to 50 °C in He. FT-IR spectra after heating the sample in He at (b) 200, (c) 400, and (d) 900 °C.

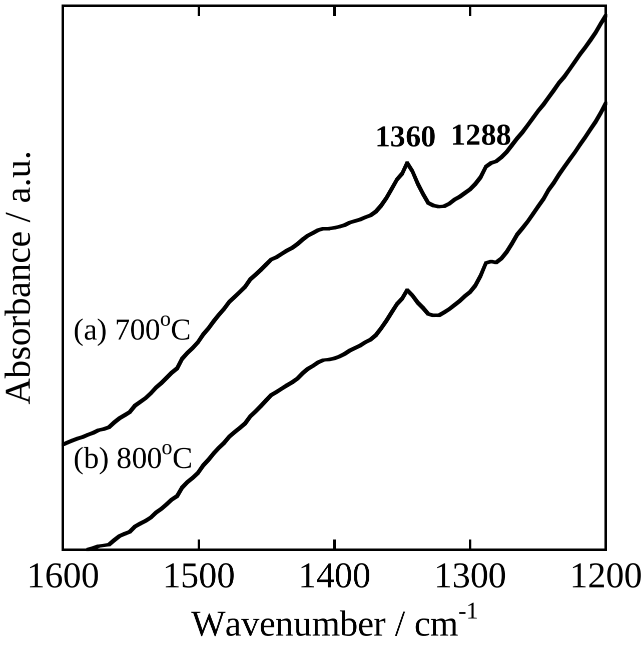

Figure 3.2 DRIFT-IR spectra of $(Y_{0.69}Tb_{0.30}Ba_{0.01})_2O_{2.99+\delta}$ in a flow of 1 vol% NO/He at (a) 700 and (b) 800 °C.

Figure 3.3 shows NO_x-TPD profiles for $(Y_{0.69}Tb_{0.30}Ba_{0.01})_2O_{2.99+\delta}$, where the samples were pretreated in a flow of 1 vol% NO/He for 30 min at 600 °C and subsequently cooled down to 50 °C. Four desorption profiles corresponding to N_2O, NO_2, NO, and O_2 were observed. The NO desorption peaks were detected in two temperature ranges: less than 400 °C and between 400 to 650 °C. The former was attributed to the desorption of adsorbed nitrosyl, while the latter was corresponded to the desorption of NO produced by the decomposition of unidentate nitrate ($NO_{3ad} \rightarrow NO_g + O_{2g}$). In fact, the O_2 desorption was also observed at the same temperature range. At high temperatures above 600 °C, the N_2O desorption became dominant, while small and broad desorption peak of NO_2 was also observed. Taking into account of the results of DRIFT-IR, N_2O and NO_2 were produced by the decomposition of adsorbed nitrosyl and unidentate nitrate. However, even at temperatures above 600 °C, N_2 desorption was not detected from the catalysts, although $(Y_{0.69}Tb_{0.30}Ba_{0.01})_2O_{2.99+\delta}$ did exhibit high NO decomposition activity in a flow of 1 vol% NO/He. These results elucidate that nitrogen is not produced by the reaction between the adsorbed species.

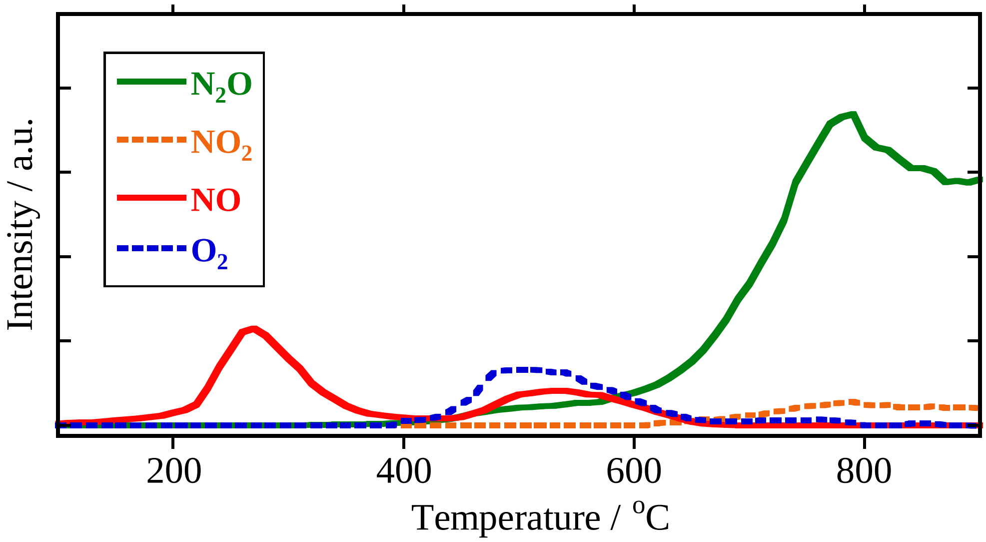

Figure 3.3 N_2O, NO_2, NO, and O_2 desorption profiles (NO_x-TPD) for $(Y_{0.69}Tb_{0.30}Ba_{0.01})_2O_{2.99+\delta}$ exposed to 1 vol% NO/He for 30 min at 600 °C.

From these results, a reaction mechanism can be proposed for direct NO decomposition on the catalysts based on C-type cubic REOs. In the first step, gaseous NO adsorbs onto the rare earth ions of the catalyst surface to form nitrosyl and bidentate nitrate species, where the relative amount of the nitrosyl is higher than that of the bidentate nitrate. In this step, the adsorbed NO molecules are reduced to nitrosyl by the electrons produced in the O_2 desorption process accompanied by the NO adsorption. Dissolution of alkaline earth metal ions in the catalyst lattice facilitates the oxidation of the nitrosyl to unidentate nitrate to produce oxide anion vacancies even at room temperature. In the elevated temperature process up to 400 °C, the unidentate nitrate is decomposed into nitrosyl again to release oxygen. When the catalyst is heated up to 600 °C, surface oxide anions desorb spontaneously as oxygen molecules leaving some oxide anion vacancies (**Fig. 3.3**). Consequently, only nitrosyl groups can exist stably on the catalyst surface above 600 °C, at which temperature the C-type cubic REOs exhibit catalytic activities for the direct NO decomposition. Since nitrogen was not produced by the reaction between the adsorbed species as mentioned above, it can be concluded that the direct NO decomposition proceeds by the reaction of adsorbed NO_x species with gas-phase NO to form N_2 and O_2 at high temperatures. The overall reaction mechanism is summarized in **Scheme 1**.

In this mechanism, surface basic sites play an important role in NO adsorption (Step 1), because the amount of nitrosyl increases with the increase in that of the surface basic sites (**Figure 1.5**). Furthermore, oxide anion vacancies are necessary for NO decomposition. Therefore, the introduction of Ba^{2+} into the lattice is effective in enhancing catalytic activity, because both the number of basic sites and oxide anion vacancies are increased, which should significantly facilitate NO adsorption. The presence of $Tb^{3+/4+}$ in the lattice accelerates O_2 desorption from the catalyst surface to promote regeneration of oxide anion vacancies by its redox properties.

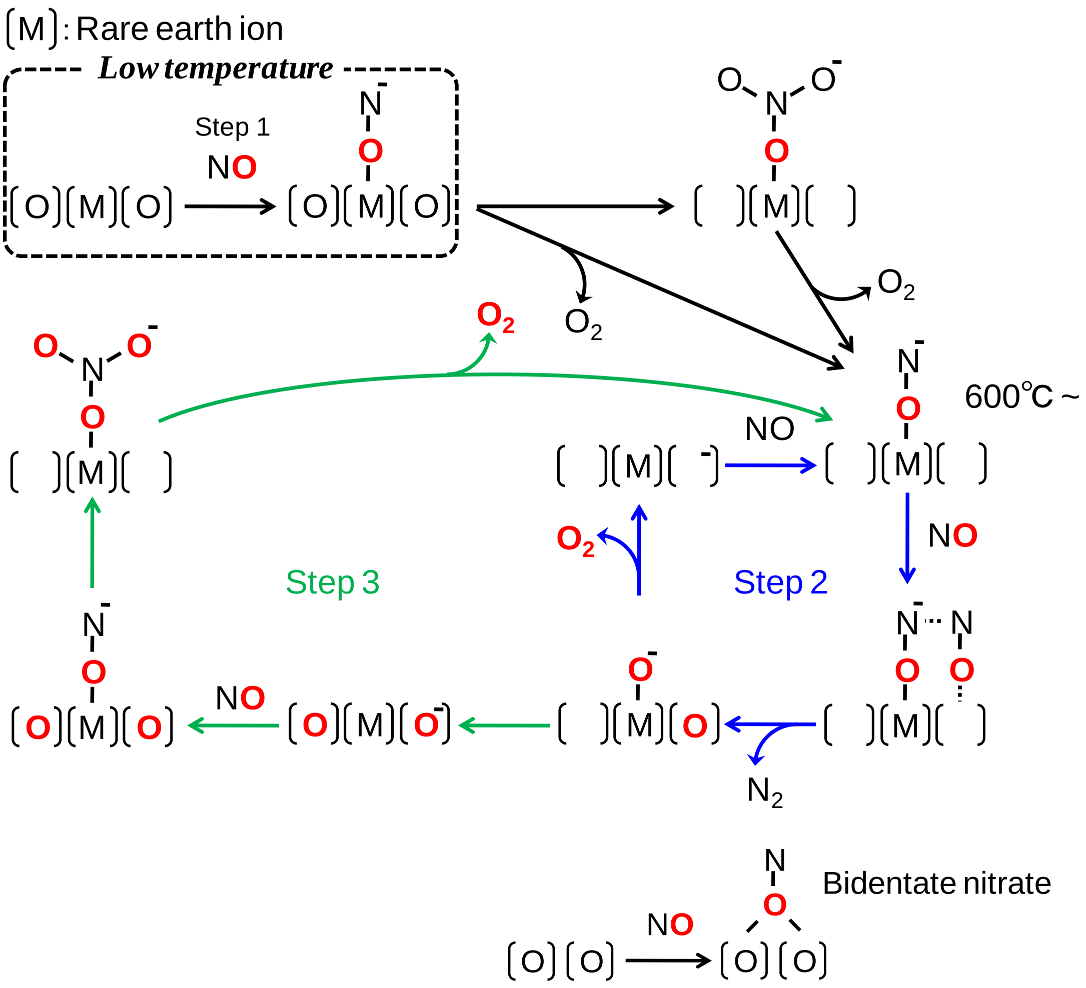

Scheme 1 Overall reaction mechanism for direct NO decomposition on a C-type cubic rare earth oxide-based catalyst.

At high temperatures above 600 °C, NO molecules in gas-phase were trapped onto the oxide anion vacancies adjacent to adsorbed nitrosyl. Then, the NO molecule reacts with nitrosyl to produce N_2 leaving two oxide anions (Step 2). These steps will proceed simultaneously, because only nitrosyl and unidentate nitrate are observed in DRIFT-IR spectra (**Figure 3.2**). In this regard, there is a possibility that the NO_x species like the *cis* hyponitrite ion (N_2O_2) are presented on the surface of the catalyst, but it is difficult to observe N_2O_2 by DRIFT-IR, because black-body radiation overlaps with the characteristic peaks of N_2O_2 such as symmetric and anti-symmetric stretch vibrations of NO at around 1138 cm^{-1} and 822 cm^{-1}, respectively.

As mentioned above, the formation of unidentate nitrate was also confirmed by the DRIFT-IR measurements, indicating that a fraction of adsorbed nitrosyl was oxidized to unidentate nitrate at high temperatures. However, the produced unidentate nitrate is decomposed into nitrosyl immediately (Step 3), and then, the nitrosyl species reacts with the gas-phase NO to form N_2 and O_2 in the regular catalytic cycle (Step 2).

3.4 Conclusions

In this chapter, a reaction mechanism has been proposed for direct NO decomposition over the REOs-based catalysts. The NO molecule adsorbed as a nitrosyl species reacts with gas-phase NO to form N_2 and O_2 on the surface of the catalysts at high temperatures. In this mechanism, the presence of Ba^{2+} in the lattice facilitates NO adsorption step, because partial substitution of the trivalent rare earth cations with divalent Ba^{2+} increases the amount of oxide anion vacancies and strong surface basic sites. In addition, the redox reaction of Tb^{3+}/Tb^{4+} promotes regeneration of oxide anion vacancies. Therefore, the double doping of Ba^{2+} and $Tb^{3+/4+}$ is effective for improving NO decomposition activity.

Chapter 4 Evaluation of Catalytic Activity for Direct NO Decomposition over C-type Cubic REOs-Based Catalysts and Synthesis of Advanced Catalysts to Inhibit Catalyst Poisoning by O_2 and CO_2

4.1 Introduction

For the application to the actual NO removal process from the automobile exhaust gas in the future, the high NO removal rate should be sustained at a high space velocity. However, the NO decomposition activity is generally lowered with increasing the space velocity, because it is considered that the reaction rate of the direct NO decomposition reaction is significantly slower than that of the selective catalytic reduction. Furthermore, there is a significant issue in the conventional direct NO decomposition catalysts that the activity decreases in the presence of O_2 and CO_2 because of catalyst poisoning.

In this chapter, therefore, the effects of the high space velocity and the presence of O_2 or CO_2 on NO conversion to N_2 over the $(Y_{0.69}Tb_{0.30}Ba_{0.01})_2O_{2.99+\delta}$ catalyst were evaluated. Furthermore, some advanced catalysts to inhibit catalyst poisoning by O_2 and CO_2 were produced for the direct NO decomposition in the presence of them.

4.2 Experimental Procedure

The C-type cubic $(Y_{0.69}Tb_{0.30}Ba_{0.01})_2O_{2.99+\delta}$, $(Yb_{0.50}Tb_{0.50})_2O_{3+\delta}$, $(Ho_{0.87}Zr_{0.05}Pr_{0.08})_2O_{3.05+\delta}$, and $(Y_{1-x}Pr_x)_2O_{3+\delta}$ $(0 \leq x \leq 0.20)$ solid solutions were synthesized by the carbonate co-precipitation method. A stoichiometric mixture of 1.0 mol dm^{-3} R(NO_3)$_3$ (R: Ho, Y, and Yb), 0.5 mol dm^{-3} Pr(NO_3)$_3$, 0.1 mol dm^{-3} Tb(NO_3)$_3$, and 0.1 mol dm^{-3} ZrO(NO_3)$_2$ aqueous solutions was added to a 1.0 mol dm^{-3} ammonium carbonate solution with stirring, and the total amount of cations was adjusted to be 10 mmol. In the case of $(Ho_{0.87}Zr_{0.05}Pr_{0.08})_2O_{3.05+\delta}$, the mixture was cooled by an ice bath with stirring. The pH of the mixture was adjusted to 10 by dropwise addition of ammonia solution. After stirring for 6 h, the resulting precipitate was collected by filtration, washed several times with deionized water, and then dried at 80 °C for 6 h. The powder was then ground in an agate mortar and finally calicined at 900 °C in air for 6 h.

The catalytic tests were carried out in a conventional fixed-bed flow reactor with a 10 mm diameter quartz glass tube. A gas mixture of 1.0 vol% NO and He (balance) was flowed over 0.5 g of catalyst at a rate of 10 − 40 cm^3 min^{-1}. The *W/F* ratio, corresponding to the space velocity, was controlled in the range between 0.75 and 3.0 g s cm^{-3}. The gas composition was analyzed using a gas chromatograph (Shimadzu, GC-8A) with a thermal conductivity detector (TCD), and a molecular sieve 5A column for NO, N_2, and O_2 separation. The activity of each catalyst was evaluated in terms of NO conversion to N_2. The effects of the presence of O_2 and CO_2 were ascertained by adding each gas species into the reactant gas. The concentrations of the added gases and NO were controlled by varying the feed rate of each gas species so as to maintain a total reactant gas flow rate of 10 cm^3 min^{-1}.

4.3 Results and Discussion

Figure 4.1 shows the space velocity dependence of NO conversion to N_2 over $(Y_{0.69}Tb_{0.30}Ba_{0.01})_2O_{2.99+\delta}$ at 900 °C. Although the catalytic activity decreased with increasing the space velocity, high N_2 yield of 80 % was sustained even at a high space velocity of 0.75 g s cm^{-3}. However, further enhancement of NO decomposition activity is considered necessary to the present catalysts, because the deNO$_x$ catalysts in practical use are requested to show high activities even at 3.6×10^{-6} g s cm^{-3} [32].

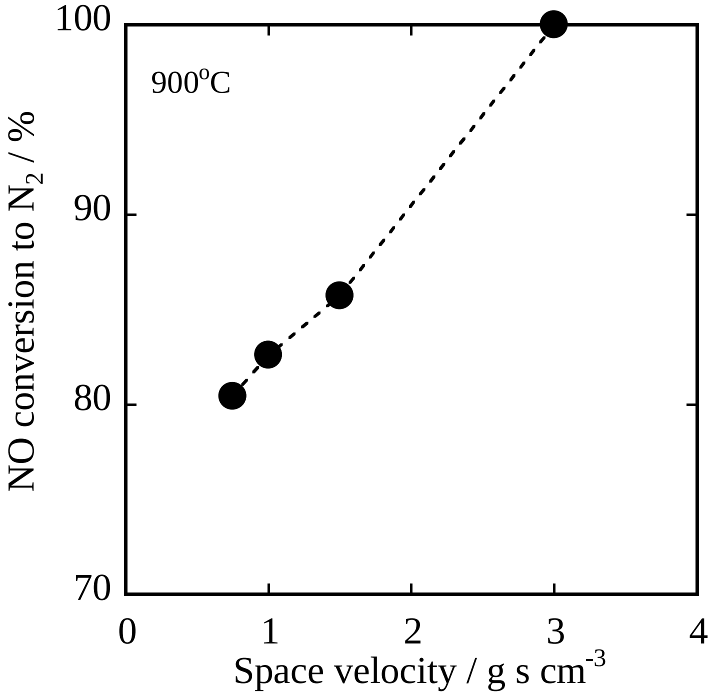

Figure 4.1 Space velocity dependence of NO conversion to N$_2$ over $(Y_{0.69}Tb_{0.30}Ba_{0.01})_2O_{2.99+\delta}$ at 900 °C (NO: 1vol%, He balance).

The effects of the presence of CO$_2$ or O$_2$ on NO conversion to N$_2$ over $(Y_{0.69}Tb_{0.30}Ba_{0.01})_2O_{2.99+\delta}$ at 900 °C are presented in **Figure 4.2** with that on a conventional perovskite-type $Ba_{0.8}La_{0.2}Mn_{0.8}Mg_{0.2}O_3$ catalyst (850 °C) [32, 57]. These data show that the negative effects of CO$_2$ and O$_2$ poisoning are reduced over $(Y_{0.69}Tb_{0.30}Ba_{0.01})_2O_{2.99+\delta}$ compared to those of the conventional perovskite-type catalysts. Actually, a high N$_2$ yield of 46 % was sustained even in the presence of 5 vol% CO$_2$. This yield is significantly higher than that observed with $Ba_{0.8}La_{0.2}Mn_{0.8}Mg_{0.2}O_3$ (18 %) in the presence of 5 vol% CO$_2$. Even in the presence of 10 vol% CO$_2$, N$_2$ yield was sustained as high as 49 % over the $(Y_{0.69}Tb_{0.30}Ba_{0.01})_2O_{2.99+\delta}$ catalyst.

Upon the addition of 5 vol% O_2, the N_2 yield (71 %) is also higher than the yield obtained from $Ba_{0.8}La_{0.2}Mn_{0.8}Mg_{0.2}O_3$ (40 %). The decrease in the N_2 yield on going from 0 to 5 vol% O_2 was only 29 % (100 % → 71 %), which is less than the decrease exhibited by $Ba_{0.8}La_{0.2}Mn_{0.8}Mg_{0.2}O_3$ under the same condition (35%; 75 % → 40 %). In addition, the $(Y_{0.69}Tb_{0.30}Ba_{0.01})_2O_{2.99+\delta}$ catalyst could maintain high N_2 yield of 64 % even in the presence of 10 vol% O_2. These results elucidate that the $(Y_{0.69}Tb_{0.30}Ba_{0.01})_2O_{2.99+\delta}$ catalyst possesses relatively high resistance to the poisoning effects of O_2 or CO_2. However, the CO_2 poisoning is still serious on the catalyst, because CO_2 is strongly adsorbed on the Ba^{2+} sites on the surface of the catalyst.

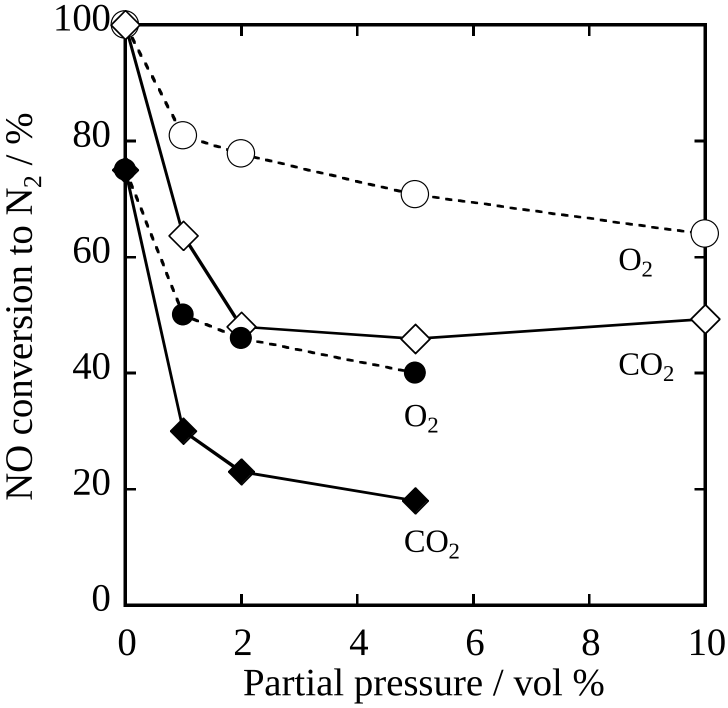

Figure 4.2 The effects of the presence of O_2 or CO_2 on catalytic activity of $(Y_{0.69}Tb_{0.30}Ba_{0.01})_2O_{2.99+\delta}$ (900 °C; open symbols) and $Ba_{0.8}La_{0.2}Mn_{0.8}Mg_{0.2}O_3$ (850 °C; closed symbols).

To address this issue, novel C-type cubic $(Yb_{0.50}Tb_{0.50})_2O_{3+\delta}$, $(Ho_{0.87}Zr_{0.05}Pr_{0.08})_2O_{3.05+\delta}$, and $(Y_{0.90}Pr_{0.10})_2O_{3+\delta}$ catalysts were designed and synthesized by co-precipitation of the corresponding carbonates similarly in the previous chapters. These catalysts are composed almost entirely of rare earth ions, purposely excluding alkaline earth ions such as Ba^{2+} and Sr^{2+} from the catalyst lattice. The effects of the presence of O_2 and CO_2 on the NO conversion to N_2 over these catalysts at 900 °C are presented in **Figure 4.3**.

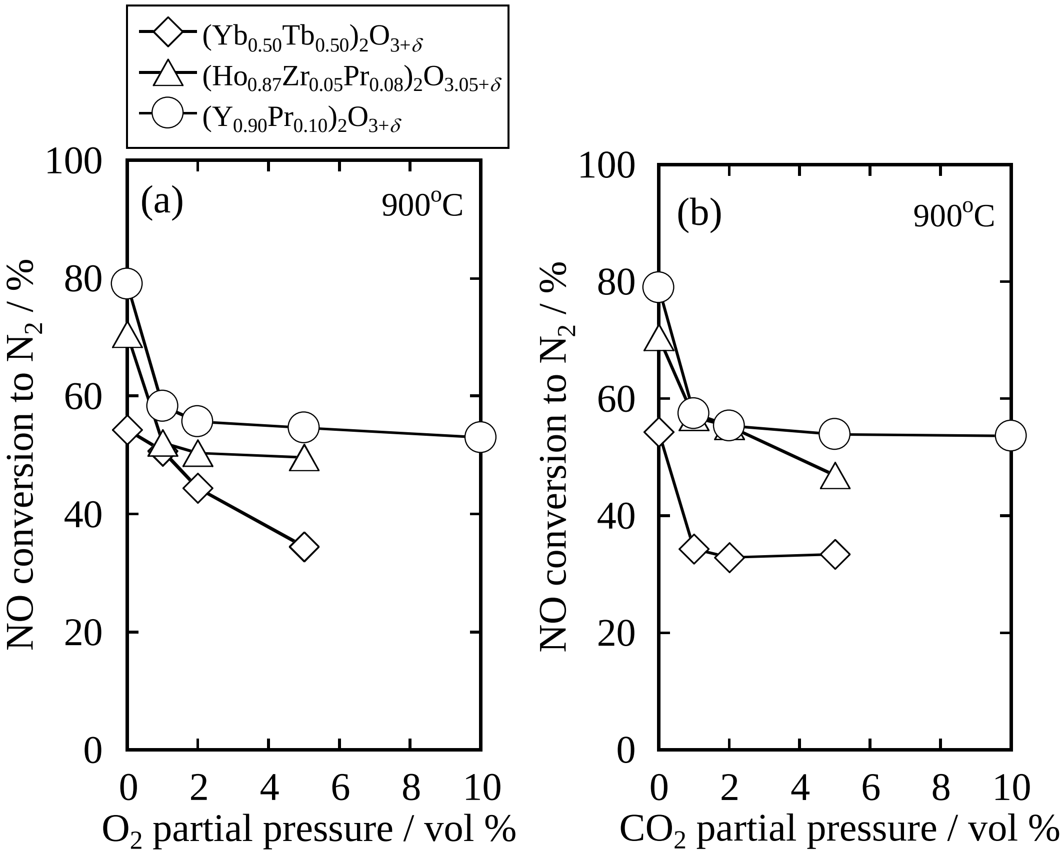

Figure 4.3 Effects of O_2 (a) and CO_2 (b) on the N_2 yield obtained over $(Yb_{0.50}Tb_{0.50})_2O_{3+\delta}$, $(Ho_{0.87}Zr_{0.05}Pr_{0.08})_2O_{3.05+\delta}$, and $(Y_{0.90}Pr_{0.10})_2O_{3+\delta}$.

These data show that the negative effects of CO_2 poisoning are reduced over these catalysts, such that those are comparable to those of O_2 poisoning. Among the samples synthesized, the highest catalytic activity was obtained for the $(Y_{0.90}Pr_{0.10})_2O_{3+\delta}$ catalyst. On this catalyst, a high N_2 yield of 53 % was obtained even in the presence of 10 vol% CO_2. This yield is higher than that observed with $(Y_{0.90}Tb_{0.30}Ba_{0.01})_2O_{2.99+\delta}$ (49 %) in the presence of 10 vol% CO_2. Upon the addition of 10 vol% O_2, the N_2 yield (53 %) was somewhat less than that of $(Y_{0.69}Tb_{0.30}Ba_{0.01})_2O_{2.99+\delta}$ (64 %). However, the decrease in the N_2 yield on going from 0 to 10 vol% O_2 was only 26 % (79 % → 53 %) with the present $(Y_{0.90}Pr_{0.10})_2O_{3+\delta}$ catalyst, which is significantly less than the decrease exhibited by $(Y_{0.69}Tb_{0.30}Ba_{0.01})_2O_{2.99+\delta}$ under the same conditions (36 %; 100 % → 64 %). Therefore, it can be concluded that, compared to the conventional Ba-containing catalysts, the $(Y_{0.90}Pr_{0.10})_2O_{3+\delta}$ catalyst possesses remarkable resistance to the poisoning effects of not only CO_2 but also O_2.

4.4 Conclusions

The $(Y_{0.69}Tb_{0.30}Ba_{0.01})_2O_{2.99+\delta}$ catalyst could maintain high NO decomposition activity at a high space velocity (W/F = 0.75 g s cm^{-3}) and in the presence of CO_2 or O_2 (W/F = 3.0 g s cm^{-3}). In addition, C-type cubic $(Yb_{0.50}Tb_{0.50})_2O_{3+\delta}$, $(Ho_{0.87}Zr_{0.05}Pr_{0.08})_2O_{3.05+\delta}$, and $(Y_{0.90}Pr_{0.10})_2O_{3+\delta}$ catalysts were synthesized to inhibit catalyst poisoning by O_2 and CO_2 on direct NO decomposition. These catalysts are composed almost entirely of rare earth ions, purposely excluding alkaline earth ions such as Ba^{2+} and Sr^{2+} from the catalyst lattice. The highest catalytic activity was obtained with $(Y_{0.90}Pr_{0.10})_2O_{3+\delta}$, which maintained significant catalytic activity even in the presence of coexisting gases.

Summary

In the work of this thesis, the fundamental factors and the effects of the Ba^{2+} and $Tb^{3+/4+}$ addition were elucidated for the C-type cubic REOs to show high direct NO decomposition activities. Furthermore, the reaction mechanism was proposed on the direct NO decomposition catalysis over C-type cubic REOs. The results obtained through this work are summarized as follows:

Chapter 1

The crystal structure is the most important factor to promote direct NO decomposition on REOs, because adsorptive capability for NO highly depends on the coordination environment of the rare earth cation in its crystal lattice. In the series of the C-type cubic REOs, the NO decomposition activity depends on the morphology of the particles correlating with the crystallinity of the REOs. The particle morphology depends on the lattice parameter of the C-type cubic REOs, and the plate-like oxides of high crystallinity show relatively high activities. The pseudo agglomeration should be the reason for the formation of plate-like oxides, and the catalytic activity increases with increasing the amount of the surface basic sites when the oxides have the same morphology.

Chapter 2

Partial substitution of trivalent rare earth cations in C-type cubic REOs with divalent alkaline earth metal ions (Ba^{2+}, Sr^{2+}, and Ca^{2+}) increases the number of oxide anion vacancies and surface basic sites to facilitate NO adsorption. The introduction of

$Tb^{3+/4+}$ into the catalyst lattice is effective to facilitate O_2 desorption from the surface, leading to the regeneration of the oxide anion vacancies. Therefore, the double doping of Ba^{2+} and $Tb^{3+/4+}$ is significantly effective for improving the NO decomposition activity, and, as a result, the significantly high activity (100% NO decomposition) was realized.

Chapter 3

A reaction mechanism has been proposed on the direct NO decomposition over the catalyst based on C-type cubic Y_2O_3. From the NO_x-TPD and DRIFT-IR measurements, it has been elucidated that only nitrosyl species can exist stably on the catalyst surface above 600 °C, and the nitrosyl species reacts with gas-phase NO to form N_2 and O_2 on the surface of the catalysts at high temperatures.

Chapter 4

The negative effects of CO_2 and O_2 on the $(Y_{0.69}Tb_{0.30}Ba_{0.01})_2O_{2.99+\delta}$ catalyst are significantly lower than those of the conventional perovskite-type catalyst. In addition, novel C-type cubic REO catalysts have been synthesized to inhibit catalyst poisoning by O_2 and CO_2, and the $(Y_{0.90}Pr_{0.10})_2O_{3+\delta}$ catalyst possesses remarkable resistance to the poisoning effects of not only CO_2 but also O_2.

References

[1] M.G. Mustafa, *Free Radical Biol. Med.*, 1990, **9**, 245–265.

[2] D.G. Streets, S.T. Waldhoff, *Atmos. Environ.*, 2000, **34**, 363–374.

[3] P. Forzatti, *Appl. Catal. A: Gen*, 2001, **222**, 221–236.

[4] N. Takahashi, H. Shinjoh, T. Iijima, T. Suzuki, K. Yamazaki, K. Yokota, H. Suzuki, N. Miyoshi, S. Matsumoto, T. Tanizawa, T. Tanaka, S. Tateishi, K. Kasahara, *Catal. Today*, 1996, **27**, 63–69.

[5] C.K. Narula, C.S. Daw, J.W. Hoard, T. Hammer, *J. Appl. Ceram. Technol.*, 2005, **2**, 452–466.

[6] G. Busca, L. Lietti, G. Ramis, F. Berti, *Appl. Catal. B: Environ.*, 1998, **18**, 1–36.

[7] N.Y. Topsoe, H. Topsoe, J.A. Dumesic, *J. Catal.*, 1995, **151**, 226–240.

[8] N.Y. Topsoe, J.A. Dumesic, H. Topsoe, *J. Catal.*, 1995, **151**, 241–252.

[9] C. Ciardelli, I. Nova, E. Tronconi, D. Chatterjee, B. Bandl-Konrad, M. Weibel, B. Krutzsch, *Appl. Catal. B: Environ.*, 2007, **70**, 80–90.

[10] I. Nova, C. Ciardelli, E. Tronconi, D. Chatterjee, B. Bandl-Konrad, *Catal. Today*, 2006, **114**, 3–12.

[11] A. Grossale, I. Nova, E. Tronconi, *Catal. Today*, 2008, **136**, 18–27.

[12] K. Rahkamaa-Tolonen, T. Maunula, M. Lomma, M. Huuhtanen, R.L. Keiski, *Catal. Today*, 2005, **100**, 217–222.

[13] S. Brandenberger, O. Kröcher, A. Tissler, R. Althoff, *Catal. Rev. Sci. Eng.*, 2008, **50**, 492–531.

[14] M. Koebel, M. Elsener, M. Kleemann, *Catal. Today*, 2000, **59**, 335–345.

[15] S.D. Yim, S.J. Kim, J.H. Baik, I.-S. Nam, Y.S. Mok, J.-H. Lee, B.K. Cho, S.H. Oh, *Ind. Eng. Chem. Res.*, 2004, **43**, 4856–4863.

[16] P.L.T. Gabrielsson, *Top. Catal.*, 2004, **28**, 177–184.

[17] Y. Murata, S. Tokui, S. Watanabe, K. Takeshita, Y. Daisho, H. Suzuki, H. Ishii, *Rev. Auto. Eng.*, 2009, **30**, 19–26.

[18] P. Granger, V.I. Parvulescu, *Chem. Rev.*, 2011, **111**, 3155–3207.

[19] M. Iwamoto, H. Hamada, *Catal. Today*, 1991, **10**, 57–71.

[20] T. Ishihara, M. Ando, K. Sada, K. Takiishi, K. Yamada, H. Nishiguchi, Y. Takita, *J. Catal.*, 2003, **220**, 104–114.

[21] Y. Teraoka, T. Harada, S. Kagawa, *J. Chem. Soc., Faraday Trans.*, 1998, **94**, 1887–1891.

[22] J. Zhu, D. Xiao, J. Li, X. Yang, Y. Wu, *J. Mol. Catal. A*, 2005, **234**, 99–105.

[23] N. Imanaka, T. Masui, H. Masaki, *Adv. Mater.*, 2007, **19**, 3660–3663.

[24] H. Masaki, T. Masui, N. Imanaka, *J. Alloys Compd.*, 2008, **451**, 406–409.

[25] G. Adachi, N. Imanaka, *Chem. Rev.*, 1998, **98**, 1479–1514.

[26] L. Pauling, *Z. Krystallogr.*, 1928, **69**, 415–421.

[27] R.M. Douglass, E. Staritzky, *Anal. Chem.*, 1956, **28**, 552–552.

[28] L. Pauling, M.D. Shappell, *Z. Kristallogr.*, 1930, **75**, 128–142.

[29] N. Imanaka, T. Masui, Y. Kato, *J. Solid State Chem.*, 2005, **178**, 395–398.

[30] M. Nagao, H. Hamano, K. Hirata, R. Kumashiro, Y. Kuroda, *Langmuir*, 2003, **19**, 9201–9209.

[31] V.A. Lysenko, *Inorg. Mater.*, 2011, **47**, 759–762.

[32] H. Iwakuni, Y. Shinmyou, H. Yano, H. Matsumoto, T. Ishihara, *Appl. Catal. B: Environ.*, 2007, **74**, 299–306.

[33] R.M. Talyshinskii, R.R. Aliev, A.A. Mkrtychev, *Chem. Technol. Fuels Oils*, 2005, **41**, 60–65.

[34] S. Pathan, A. Patel, *Dalton Trans.*, 2011, **40**, 348–355.

[35] P.B. Venuto, *Microporous Mater.*, 1994, **2**, 297–411.

[36] N. Singhania, E.A. Anumol, N. Ravishankar, G. Madras, *Dalton Trans.*, 2013, **42**, 15343–15354.

[37] N.A. Barakat, M.A. Adbelkareem, M. El-Newehy, H.Y. Kim, *Nanoscale Res. Lett.*, 2013, **8**, 402–408.

[38] X. Xie, Y. Li, Z.Q. Liu, M. Haruta, W. Shen, *Nature*, 2009, **458**, 746–749.

[39] D.E. Tevault, L. Andrews, *J. Phys. Chem.*, 1973, **77**, 633–639.

[40] S.J. Huang, A.B. Walters, M.A. Vannice, *J. Catal.*, 2000, **192**, 29–47.

[41] G. Busca, V. Lorenzelli, *Mater. Chem.*, 1982, **7**, 89–126.

[42] J. Wang, H. Song, B. Sun, X. Ren, B. Chen, W. Xu, *Chem. Phys. Lett.*, 2003, **379**, 507–511.

[43] V. Singh, V.K. Rai, I. Ledoux-Rak, S. Watanabe, T.K. Gundu Rao, J.F.D. Chunbaci, L. Badie, F. Pelle, S. Ivanova, *J. Phys. D: Appl. Phys.*, 2009, **42**, 065104.

[44] X.L. Jing, Q.C. Chen, C. He, X.Q. Zhu, W.Z. Weng, W.S. Xia, H.L. Wan, *Phys. Chem. Chem. Phys.*, 2012, **14**, 6898–6904.

[45] Z. Huang, W. Guo, Y. Liu, Q. Huang, F. Tang, Y. Cao, *Mater. Chem. Phys.*, 2011, **128**, 44–49.

[46] S. Shwan, W. Partridge, J.S. Choi, L. Olsson, *Apple. Catal. B: Environ.*, 2014, **147**, 1028–1041.

[47] S.M. Mathew, S.B. Umbarkar, M.K. Dongare, *Catal. Commun.*, 2007, **8**, 1178–1182.

[48] P. Broqvist, H. Gronbeck, E. Fridell, I. Panas, *Catal. Today*, 2004, **96**, 71–78.

[49] B.M. Weiss, K.B. Caldwell, E. Iglesia, *J. Phys. Chem. C*, 2011, **115**, 6561–6570.

[50] P. Broqvist, I. Panas, E. Fridell, H. Persson, *J. Phys. Chem. B*, 2002, **106**, 137–145.

[51] R.D. Shannon, *Acta. Cryst. A*, 1976, **32**, 751–767.

[52] S. Sato, R. Takahashi, M. Kobune, H. Gotoh, *Appl. Catal., A*, 2009, **356**, 57–63.

[53] H.Z. Zhang, L.Y. Liang, A.H. Chen, Z.M. Liu, L. Yu, H.T. Cao, Q. Wan, *Appl. Phys. Lett.*, 2010, **97**, 122108.

[54] D.D. Sarma, C.N.R. Rao, J. Electron, *Spectrosc. Relat. Phenom.*, 1980, **20**, 25–45.

[55] B.M. Reddy, P. Salkia, P. Bharall, S.E. Park, M. Muhler, W. Grunert, *J. Phys. Chem. C*, 2009, **113**, 2452–2462.

[56] K. Masumoto, A. Semba, C. Kimura, T. Taniguchi, K. Watanabe, T. Sakata, H. Aoki, *Jpn. J. Appl. Phys.*, 2011, **50**, 04DH01.

[57] H. Iwakuni, Y. Shinmyou, H. Yano, K. Goto, H. Matsumoto, T. Ishihara, *Bull. Chem. Soc. Jpn.*, 2008, **81**, 1175–1182.

Acknowledgements

The author would like to express his heartfelt gratitude to Professor Dr. Nobuhito Imanaka, Department of Applied Chemistry, Graduate School of Engineering, Osaka University, for his continuous guidance, many invaluable suggestions, and his science encouragement throughout the work. The author is indebted to Dr. Toshiyuki Masui, Department of Applied Chemistry, Graduate School of Engineering, Osaka University, for his continuous guidance and stimulating discussions for carrying out this work.

The author is also very grateful to Dr. Shinji Tamura, Department of Applied Chemistry, Graduate School of Engineering, Osaka University, for his helpful suggestions and heartfelt advice.

The author is obliged to Dr. Hirokazu Izumi, Hyogo Prefectural Institute of Technology, for XPS measurements. Furthermore, the author desires to express his sincere thanks to Dr. Takao Sakata, Professor Dr. Hidehiro Yasuda, and Professor Emeritus Dr. Hirotaro Mori, Osaka University, for their assistance with the TEM measurement. In addition, the author is grateful to Dr. Toshiaki Arata, Osaka University, for his assistance with the ESR measurement.

The author is deeply grateful to Professor Dr. Ken-ichi Machida, Department of Applied Chemistry, Graduate School of Engineering, Osaka University, and Professor Dr. Yoichi Ando, Department of Applied Chemistry, Graduate School of Engineering, Osaka University, for reviewing this thesis and giving their valuable comments.

The author is also very grateful to Dr. Keisuke Yasuda, Kobe City College of Technology, for his helpful suggestions and heartfelt advice.

Special thanks should be given to author’s co-workers, Mr. Takashi Mima, Mr. Wang Xiaojing, Ms. Chiya Nishimura, Mr. Shunji Uejima, Mr. Ryosuke Nagai, Mr.

Hayato Imadzu, Mr. Takahiro Miyamoto, Mr. Atsuki Yoshimura, Mr. Kazuya Jyoko, Mr. Atsushi Katsuma, Mr. Tomoya Kamata, Mr. Min Yeong Kim, Mr. Takanobu Ono, Mr. Nashito Fukuhara, and Mr. Taihei Honda for their helpful assistance and support in the course of this work, and members of the research group under direction of Professor Dr. Nobuhito Imanaka, Osaka University.

The Japan Society for the Promotion of Science and the Steel Industry Foundation for the Advancement of Environmental Protection Technology is also acknowledged for a research fellowship.

Finally, the author is particularly grateful to my parents, Mr. Hironoshin Tsujimoto and Mrs. Kazumi Tsujimoto, and my brother, Mr. Ryojiro Tsujimoto, who have been understanding and supporting him.